



Microstructural Response of Highly Porous Sintered Nano-silver Particle Die Attachments to Thermomechanical Cycling

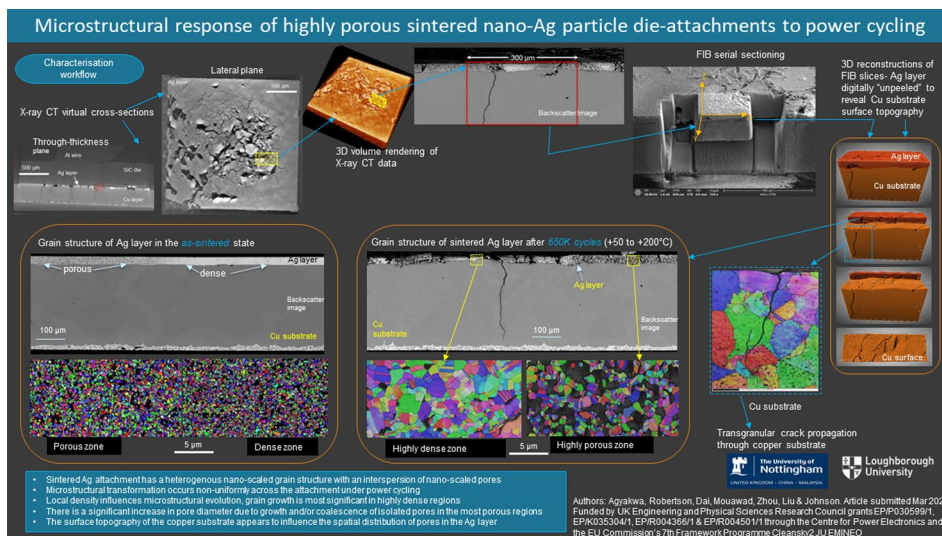
Pearl A. Agyakwa¹ · Stuart Robertson² · Jingru Dai¹ · Bassem Mouawad¹ · Zhaoxia Zhou² · Changqing Liu³ · C. Mark Johnson¹

Received: 6 March 2023 / Accepted: 30 November 2023
© The Author(s) 2024

Abstract

This paper deals with the performance of sintered nano-silver bonds used as wide-bandgap power module die attachment technology. The paper specifically explores the fine-scale microstructures of highly porous sintered attachments under power cycling to provide a deeper understanding of the significance of porosity as a reliability-related microstructural parameter. Attachments prepared at 220°C using a pressure of 6 MPa for 1 s (parameters known to generate approximately 50% porosity from previous work) and subsequently subjected to 650,000 power cycles between 50°C and 200°C are assessed. A correlative workflow integrating x-ray computed tomography, focused ion beam (FIB) and electron backscatter diffraction (EBSD) data is applied to merge meso- and nanoscale microstructural features to illuminate the degradation mechanisms. The as-sintered Ag layer has a high volume of heterogeneously distributed pores, and consists of randomly oriented equiaxed grains whose sizes vary depending on the local density of the region sampled. Power cycling promotes grain growth and the loss of twin boundaries, and these changes are more pronounced within more dense regions of the Ag attachment. In contrast, the copper substrate appears to undergo some grain refinement, with deformation twins visible within finer-grained zones during power cycling. Cracks, which appear to start off within the Ag layer, propagate across the Ag-Cu boundary and transgranularly through fine-grained regions within the copper with little tortuosity. These observations are discussed within the context of reliability behaviour.

Graphical Abstract



Extended author information available on the last page of the article

Published online: 05 January 2024

Keywords Sintered nano-silver · SiC die-attach · 3D x-ray tomography · 3D FIB/EBSD · correlative microscopy · die attachment · thermomechanical fatigue · reliability · power electronics · power cycling test

Introduction

Power electronics technologies are critical for transport electrification and renewable energy. In power semiconductor components, thermomechanical fatigue cracking of interconnections is an inevitability, because heating and cooling cycles during switching cannot be avoided. This fatigue-inducing stress is made worse because power modules require the joining together of a wide range of material types for a variety of complementary functions, but with divergent coefficients of thermal expansion.^{1–4} Soldering, the most common die attachment method, is unsuitable for many emerging wide-bandgap power electronics applications because of poor reliability at elevated temperatures and environmentally hazardous properties in some cases.⁵

Sintered silver attachments are demonstrably more stable and reliable than solder,^{6,7} and the fact that sintering can be carried out at relatively low homologous temperatures^{8–10} is hugely advantageous from a manufacturing perspective. Porosity is an inescapable outcome of sintering processes.^{11–13} Attachments manufactured under so-called pressureless conditions or moderate temperature/pressure/time profiles have complex heterogeneous porosity profiles.^{14–17} Although the occurrence and morphologies of these heterogeneous pore structures are thought to be largely stochastic,^{11,17} clear patterns have been observed in their spatial distribution/localisation and substrate surface topography.^{14,15} Several studies have looked at how processing parameters and initial porosity affect mechanical properties^{18–20} and thermal conductivity.^{21,22} The relationship between (declining) mechanical strength and porosity is said to be approximately linear for sintered Ag bulk specimens.¹⁹ Sintering temperature has been shown to influence crack propagation rate under isothermal mechanical fatigue,²³ including theoretical modelling and analysis of the effects of simplified pore morphologies.¹¹

However, little is still known about how these complex pore structures and networks evolve under anisothermal fatigue, i.e., stress conditions more representative of operation in a power electronics context. In theory, and perhaps contrary to the common assumption, porosity is not necessarily a disadvantage from a fatigue perspective, depending on morphology.¹² However, porosity has been linked with the formation and propagation of cracks within these attachments.^{15,23} Continued densification during temperature cycling has been suggested as a mechanism through which cracks are formed.^{14,15} The driving force for this is

the achievement of a reduction of internal surface area of the pores and is understood to be inversely proportional to their radius of curvature.²⁴ This may explain the greater extent of densification observed in specimens with higher initial levels of porosity in.¹⁵ Like all damage phenomena, this proposed mechanism has its origins in the fine-scale structure-property relationships of the sintered silver and copper substrate layers. However, these remain relatively unexplored. Understanding of the crystallography of damage evolution is vital to the development of constitutive lifetime models to support design for reliability and sustainability. These gaps in our current knowledge are in part due to the practical challenges associated with nanoscale characterisation, which can be a significant impediment to realising this timely information. For example, standard metallurgical preparation techniques often severely compromise the efficacy of analysis of sintered material because of smearing, smudging and deformation of pores/cracks.

Recent advances in our understanding of the degradation mechanism of sintered attachments under power cycling have been aided by the unique cross-sectional perspectives in the lateral plane afforded by 3D x-ray tomography.^{7,14,15,25} This way of looking at sintered attachments has allowed us to recognise its analogy to other shrinkage-cracking phenomena both in the natural world and in engineering,²⁶ thus expediting understanding of the mechanistics of physical degradation under operation. This ‘lateral plane’ frame of reference would be ordinarily unfeasible through standard metallurgical sectioning approaches alone, where through-thickness perspectives are the norm. The new insights highlight the value and importance of further scrutiny in these alternative (3D) perspectives, and partly motivate our goal of realising fine-scale microstructural observations in the lateral plane.

Research activities around sintered nanoAg die attachments tend to be aimed toward achieving highly dense structures (< 10% porosity) and therefore require sintering temperatures exceeding 250°C for durations up to 30 min.^{10,27,28} However, to ensure compatibility with other power module packaging processes, there is justification for the development of robust and reliable Ag sintered attachments with shorter processing times at lower temperatures and pressures. Although such conditions inevitably produce high-porosity joints with lower shear strength,²⁹ these are still demonstrably more robust than some of the most reliable solder alloy attachments under power cycling.^{14,30,31} It has also been suggested their increased compliance due

to lower elastic moduli (in comparison to bulk silver) may improve a joint's capacity to absorb stresses arising from thermal expansion mismatch.¹⁶ This paper explores the fine-scale microstructures of the highly porous structures resulting from the use of such 'moderate' parameters, and how these are altered by an extensive duration of power cycling between 50°C and 200°C. Our overall aim is to explore the relationship between the heterogeneous pore structures, crack development and local microstructure, and to identify any related crystallographic characteristics which favour or restrain crack propagation. Because of the perception of porosity as inherently disadvantageous to reliability, furthering our understanding is necessary to provide more confidence for the acceptance of these more porous attachments for power module manufacture. Electron backscatter diffraction (EBSD) and focused ion beam (FIB) tomography are utilised as tools within a correlative framework to complement the 3D tomography data upon which earlier hypotheses^{15,31} were based, to provide three-dimensional information about the microscale crystallographic aspects of damage evolution and fracture mechanics. The availability of corresponding x-ray computed tomography data for the specimens provides a 3D overview of crack formation and facilitates precise and deliberate selection of FIB and EBSD regions of interest, taking account of the crack length scales and giving sufficient context for crack networks.

Experimental

Materials and Coupon Manufacture

Test coupons were manufactured using CREE CPW4-1200-S010B SiC diodes which are 2.26 mm × 2.26 mm × 0.377 mm in size, and which have a 1.4 μm Ni/Ag metallisation on the cathode (back side) and a ~4 μm Al metallisation on the anode (top side), compatible with silver sintering and Al wire bonding processes, respectively.

The SiC diodes were sintered onto aluminium nitride ceramic substrates consisting of a 1-mm-thick AlN ceramic tile sandwiched between 0.3-mm-thick active brazed copper layers. The copper layers are finished with nickel (2–3 μm thick) and silver (0.2 μm thick) to facilitate the sintering process. A nano-silver film was used (Argomax 2020), 62.3 μm thick with an average particle size of ~ 20 nm, which was obtained from Alpha Assembly Solutions (Somerset, NJ 08873, USA).

Sintering Procedure and Parameters

The specimens explored in this paper were prepared using parameters determined from a previous parameter optimisation study.^{14,31} The sintering process was performed with a

Datacon 2200 EVO high-accuracy die bonder. The nano-silver film was first transferred onto a diode using a pick-and-place tool heated to 130°C under a pressure of 3 MPa for 1 s. The diode and film, which were now loosely attached, were then placed on a substrate tile which had been pre-heated to 220°C. A pressure of 6 MPa was then applied through the pick-and-place tool for 1 s. Following sintering, a few aluminium wires were ultrasonically bonded to provide interconnections between the anode of the diode and the appropriate track on the substrate tile. There were frequent Al wire lift-offs over the course of the power cycling experiment, due to their inferior robustness in comparison to the sintered attachment.^{32,33} In order to subject the sintered attachment to extensive power cycling, failed wires were replaced with new ones whenever a lift-off occurred, until it was no longer possible to do so. Two strips of 125 μm Ag foil were soldered onto the substrate to provide external circuit connections. Further details of the sintering process can be found in.¹⁴

Power Cycling

Specific details of the power cycling procedure have been previously reported by the authors and can also be found in earlier work.^{14,31} The cycling was performed using a Mentor Graphics® Power Tester 1500A platform, and specimens were mounted onto a water-cooled cold-plate maintained at a constant coolant temperature of 20°C. The electrical heating current was controlled to deliver minimum and maximum junction temperatures of 50°C and 200°C respectively, i.e., yielding a constant temperature amplitude of 150°C (+50 to +200°C ± 7°C). The current on and off times were 5 and 2.5 s, respectively.

In this work, two specimens sintered using the same parameters described above are compared: one in the as-sintered condition, and the other after 650,000 power cycles. This represents the number of cycles at which point degradation in the die attachment had become significant, and because of some lateral detachment, the bond force required to replace failed bond wires led to a crack in the active device. For context, 650,000 cycles under the test conditions described above represents a level of longevity significantly superior to what is ordinarily achievable using conventional solder.^{15,34,35}

X-Ray Tomography Imaging and Analysis

Imaging was carried out on a ZEISS Xradia Versa XRM 500 machine platform using a beam voltage of 160 kV and a 0.4X objective detector. Specimen-to-source and specimen-to-detector distances were chosen to enable the entire area of the sintered attachment (2.26 × 2.26 mm) to be within the field of view. This resulted in a spatial resolution of

approximately 2.3 μm , adequate for a meso-scale scrutiny of the developing features in both the sintered attachment and the copper substrate beneath. A filter was applied to the x-ray beam to minimise artefacts, and images were captured using a 2×2 camera binning mode. A total of 1601 and 2401 projection images were obtained over a rotation span of 180° for the as-sintered and cycled specimens, respectively (full specimen rotation was unnecessary due to the high aspect ratio of the test coupons). The region of interest is depicted in the schematic diagram give in Fig. 1. Further details regarding the x-ray imaging protocol can also be found in.¹⁵

The x-ray projections were reconstructed using ZEISS Xradia 3D Reconstructor software, which uses a filtered back-projection algorithm. The tomography datasets were visualised and virtually cross-sectioned using the ZEISS Xradia 3D Viewer. Further visualisation, segmentation, surface generation and semi-quantitative area and volume analyses were carried out using Avizo Fire 9.0.1 software and Dragonfly 3D (Object Resource Systems).

Correlative Serial FIB Sectioning and EBSD

To prepare the samples for cross-sectional metallographic analysis, the samples were cut with a Struers Accutom-5 cutter, equipped with a diamond blade and polymer coolant. The as-sintered sample was studied with the silicon carbide die intact while the power-cycled sample no longer had the die attached (the die had been previously systematically polished away with the intention of allowing the lateral plane of the sintered surface to be viewed optically).

Following cutting, the samples were mounted in Struers cold mounting epoxy resin to preserve the pore shape and avoid artificial aging through a hot-mounting process. Once mounted, the samples were polished using silicon carbide papers with decreasing grits from 220 to 4000 grit. After grinding, the samples were polished with 9 μm , 3 μm , 1 μm diamond suspensions. A solution of Struers Mastermet, Masterprep and water (10:10:80) was used to expose the

grain structure of the copper DBC for electron backscatter diffraction (EBSD) analysis.

Electron imaging, FIB serial sectioning, energy dispersive x-ray spectroscopy (EDS), and EBSD were all conducted in a Helios G5 p-FIB (Thermo Fisher Helios Plasma FIB) equipped with Oxford Instruments Ultim Max and Symmetry detectors (Oxford Instruments). These detectors, in combination with the high currents provided by the xenon plasma source, allow for swift serial sectioning of large volumes of material. The p-FIB source does, however, come at the cost of increased milling artifacts which can be observed in some cross sections.

For the characterisation of the grain structure of the copper substrate, large-area EBSD montage maps were collected at 20 keV and current of 13 nA with a step size of 0.5 μm and total horizontal field widths of around 2.3 mm. Linear intercept measurements were used to determine the grain size of the copper layer of the DBC below the die attachment.

For the characterisation of the as-sintered silver material, a slab lift-out procedure was used to isolate and polish the silver sinter as the geometry of the sample and silicon carbide die prevented successful polishing of the silver sinter through other means. The slab lift out was performed in the same fashion as a typical TEM lift-out with a lamellar structure ($30 \times 40 \times 8 \mu\text{m}$) being lifted from the bulk and transferred to a copper half grid. Once on the copper half grid, the sample could be polished imaged with the BSE detector and analysed with EBSD. To successfully index the fine silver grains, an accelerating voltage of 10 keV and current of 6.4 nA was used with a step size of both 20 nm and 50 nm for the as-sintered and power-cycled samples, respectively.

A correlative approach was taken for the serial sectioning process on the power-cycled sample whereby the micro-CT data were used to inform sampling location, as previously mentioned. An area with numerous long and short cracking and consistent thickness of silver was selected. For expediency, an in situ approach was taken whereby a platinum cap ($220 \mu\text{m} \times 100 \mu\text{m} \times 7 \mu\text{m}$) was deposited on

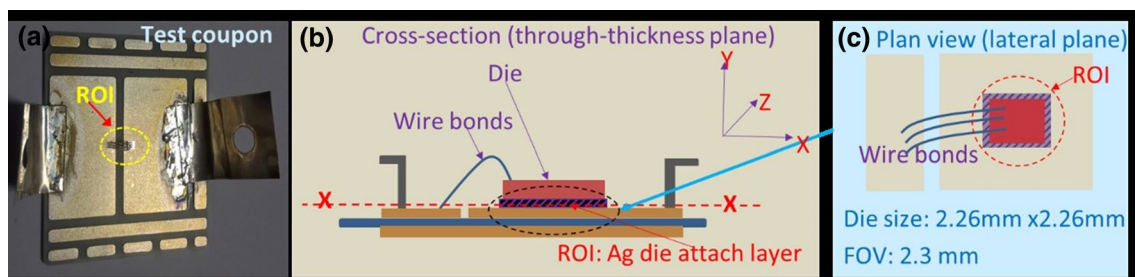


Fig. 1 (a) Test coupon, and 3D x-ray tomography field of view (FOV) and region of interest (ROI) in the (b) through-thickness (c) and lateral planes.

the surface at 16 keV. Vent cuts were then made around the perimeter of the sample and under the sample to produce an isolated volume. These cuts ensure a clear line of sight to the EBSD detector. Serial sectioning was conducted at 30 keV and 0.2 μA current, a slice thickness of 200 nm was used (see Fig. 2). Backscatter and secondary electron images

were recorded after each milling step at 5 keV and 3.2 nA with a horizontal field width of 260 μm and resolution of 1536 pixels resulting in a voxel size of 169 nm in the XY plane. The sample was mounted on a 36° pre-tilted holder and tilted to 54° for imaging, ensuring no foreshortening artifacts were produced. The brightness and contrast in the

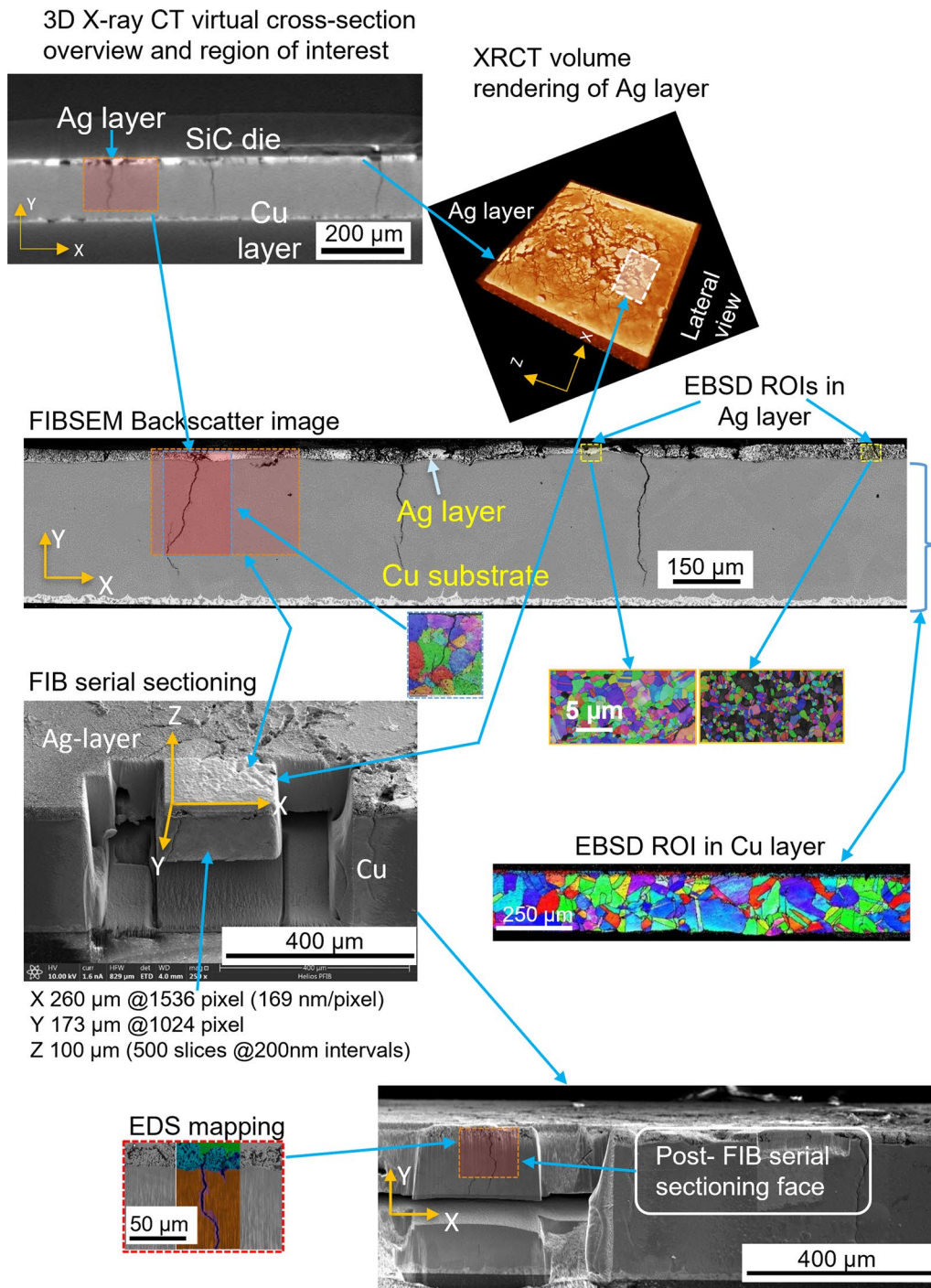


Fig. 2 Graphical model of correlative sampling for EBSD, p-FIB serial sectioning and EDS mapping. p-FIB milling was performed in the Z-direction at 200 nm intervals.

images were tuned to limit shine-through artefacts in the silver sinter layer.

The 3D reconstruction of the microstructure was performed with Dragonfly 3D (Object Resource Systems). Due to the similar atomic mass and subsequent contrast of copper, silver and platinum in the backscatter images, a neural network-based segmentation approach was used. This was iteratively implemented until an accurate model of the material was reproduced.

Results and Discussion

Overview of Structures of Sintered NanoAg Attachment Layer Pre- and Post-Cycling

In Fig. 3, overviews of the meso-structures obtained from x-ray tomography of both sintered Ag layers are presented. These show through-thickness and lateral cross-sectional views of the entire die area in both cases. There are no ‘cracks’ seen in the as-sintered specimen at this resolution ($\sim 2 \mu\text{m}$ pixel size) in the as-sintered substrate, although a few small isolated, round pores are visible (Fig. 3b). However, a texture produced from differing levels of x-ray absorption, previously reported to resemble the grain

structure of the copper substrate beneath¹⁵ can be seen. This is understood to be related to nonuniform packing density due to the substrate’s roughness. In the power-cycled specimen, numerous branched shrinkage cracks are observable (Fig. 3d), concentrated predominantly within the centre of the attachment. The pattern made by the cracks is reminiscent of absorption textures seen in the as-sintered condition (Fig. 3b).

In Fig. 4, overviews of the FIB backscattered electron cross-sectional images in the through-thickness plane of both sintered Ag layers are presented. The as-sintered and cycled Ag layers are approximately $23 \mu\text{m}$ and $27 \mu\text{m}$ thick, respectively. It is interesting to note a heterogeneous porous structure, exhibiting some highly dense as well as some highly porous regions within both specimens, although porosity is most pronounced in the cycled specimen (porosity measurements are detailed in Table I). Interestingly, and concurrent with the observations made from the virtual slices in Fig. 3, the FIBSEM images show the centre of the as-sintered Ag layer to be highly dense in contrast to the edges of the attachment. They also confirm that the cycled specimen is most porous overall, with cracks that originate within porous regions of the Ag layer propagating through the copper directly beneath.

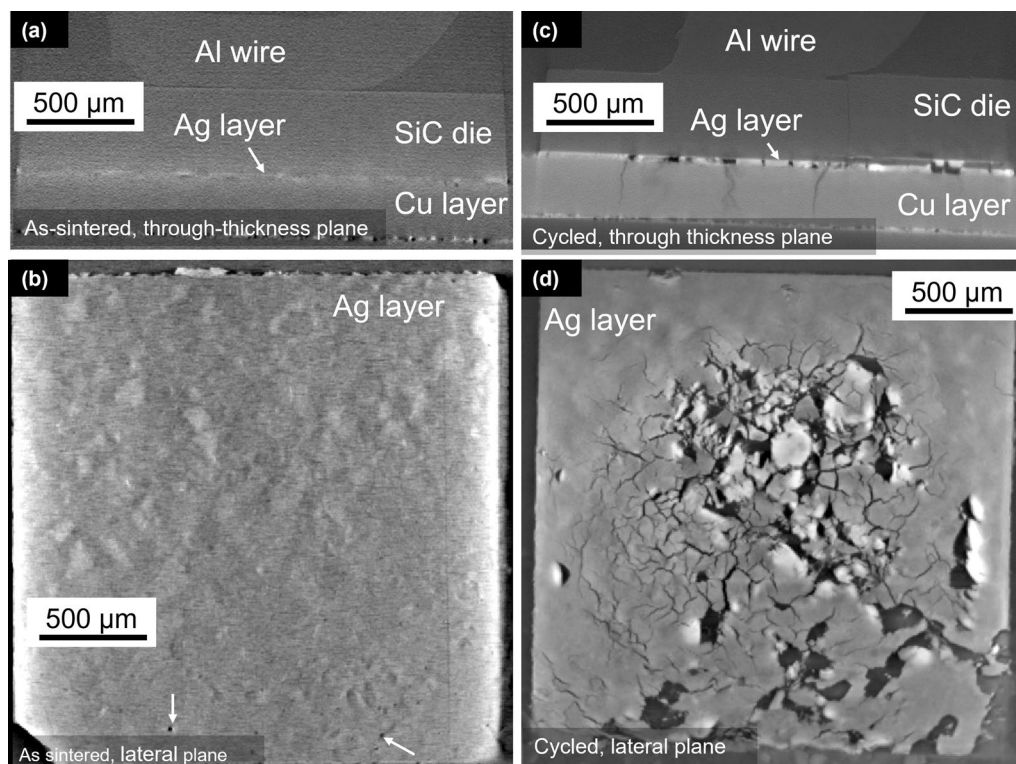


Fig. 3 3D x-ray tomography virtual slices of as-sintered and cycled Ag layers. (a, b) As-sintered sample viewed in the through-thickness and lateral planes, respectively. (c, d) Cycled sample viewed in the through-thickness and lateral planes, respectively.

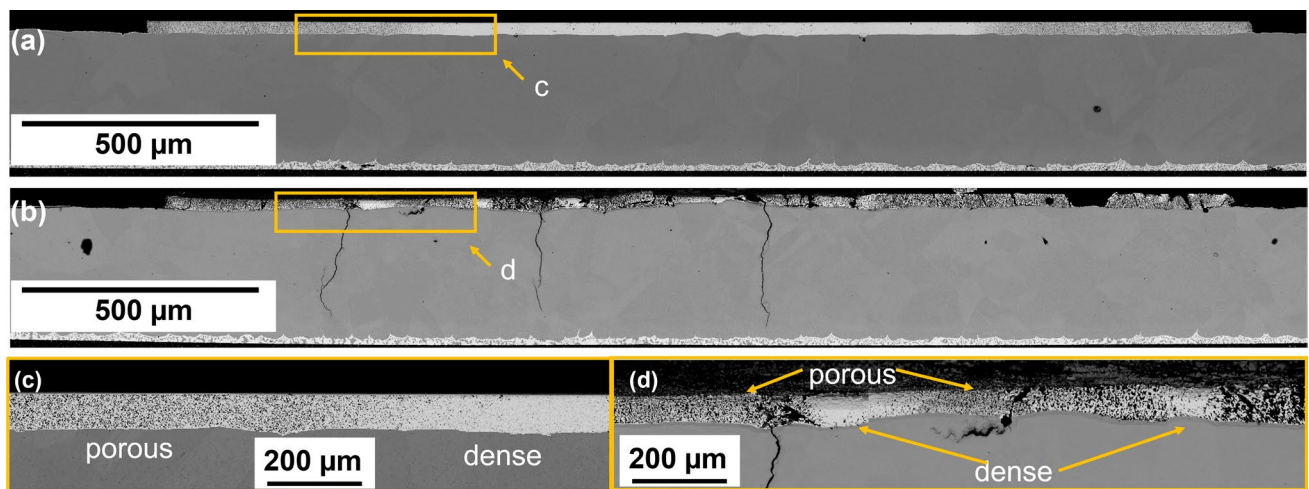


Fig. 4 Backscattered electron images of as-sintered (a, c) and cycled (b, d) samples showing regions of differing porosity.

Table 1 Porosity measurements in as-sintered and power-cycled samples

Average values	As-sintered		After power cycling (650,000 cycles, 50–200°C)		
	Porous region	Dense region	Low density	Medium density	High density
Porosity %	41	35	42.1	16	6.8
Porosity diameter (μm)	0.206	0.195	0.83	0.34	0.19 (excluding large vertical discontinuity)

These observations illustrate the idea that thermal cycling drives a process of continued (and highly localised) densification, with the by-product of increased porosity, coalescence of pores via Ostwald ripening and shrinkage cracks in ab initio low-density regions.¹⁵ Similarly heterogeneous structures are evident in the work of Chen et al.²³ which looks at SiC dies sintered onto DBC structures, and which also became more heterogeneous in porosity terms with temperature cycling. The authors attribute this variation to differing states of tension and compression within the attachment under cycling and do not explicitly consider continued densification, although it is an also plausible cause.

Compositional Profiles of the As-Sintered and Power-Cycled Attachments

The Ag-Cu interface structures can also be inspected in the backscatter images in Fig. 5. In Fig. 5a, a uniform, continuous and dense layer of bright pixels, approximately 120 nm thick (thought to be Ag), can be seen directly above the Cu substrate in the as-sintered condition. However, this layer is not observed after power cycling (Fig. 5b). In its place, there is a darker continuous layer, believed to be oxide.

To investigate further, energy dispersive spectral images are shown for the as-sintered and cycled samples in Figs. 6 and 7, respectively. In Fig. 6, energy dispersive spectral images are shown for the porous region of the as-sintered specimen. The titanium and nickel layers beneath the die are observable and measure approximately 0.14 μm and 0.81 μm , respectively. The Ag coating which finishes the back surface of the SiC die is uniform, dense and measures approximately 0.55 μm . However, the Ni layer expected above the copper DBC layer is not observed, and may have been absorbed into the Ag during the sintering process. The solid phase observed at the Cu-Ag interface in the as-sintered specimen in Fig. 5a is confirmed as Ag-rich (Fig. 6d).

There are marked changes in EDS images after 650,000 power cycles (see Fig. 7). The power-cycled sample shows prominent and continuous oxygen-rich layers, approximately $1.28 \pm 0.25 \mu\text{m}$ in thickness, coating the surfaces of cracks and large pores both within the Ag and Cu layers. A porous, oxygen-rich layer can also be observed at the interface between the Ag and Cu layers (Fig. 7f). This correlates with the line of unindexed (black) points at the Ag-Cu interface in the IPF image in Fig. 7b and resembles the dark layer observed at the Ag-Cu interface in Fig. 5b. A similar

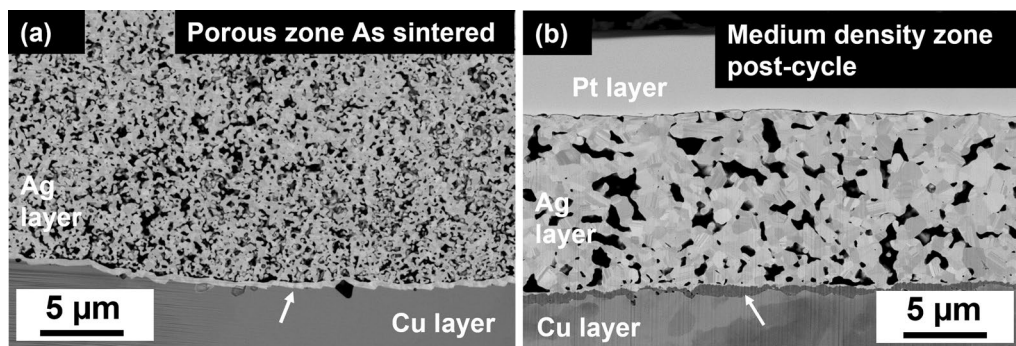


Fig. 5 Backscatter images showing the interface between the Ag sintered layer and the copper substrate for (a) a porous zone of the as-sintered specimen, and (b) the medium density zone of the cycled specimen.

observation was reported at the Ag-Cu interface during the isothermal ageing of SiC-sintered Ag-Cu attachments.³⁶ Furthermore, no EBSD patterns formed from the oxygen-rich layer which lines the large crack in the Cu layer (Fig. 7b), confirming its amorphous nature (see Fig. 7h and i). Spot semi-quantitative analysis on the crack within the copper suggests the Cu_2O stoichiometry, which is said to be consistent with Cu oxide formed below 400°C.^{36,37} Porous and cracked structures easily promote the permeation of oxygen given favourable thermodynamic and environmental conditions, leading to oxide formation.³⁸ The impact of oxide growth in the context of this work is not yet clear, as the presence and growth of oxide within crack ducts may either intensify the strain at the crack tip, resulting in an acceleration of crack growth rate, or the exact opposite, whereby a mechanical wedging action serves to reduce the local stress intensity range.³⁹ An oxide layer at the Ag-Cu interface is also likely to disrupt the thermal path between the layers, leading to increased thermal resistance.⁴⁰

Porosity Evolution in Ag Layer

To further understand these heterogeneous structures in microstructural terms, FIB/EBSD characterisation of both sintered attachments has been undertaken.

As shown earlier in Fig. 4, distinct zones in porosity terms were identifiable within both as-sintered and cycled samples. These are now shown at a higher magnification in the series of backscatter electron images in Fig. 8. There are two discernible regions within the as-sintered sample with differing levels of porosity: higher density (Fig. 8a) and higher porosity (Fig. 8b). For the cycled sample, three areas of contrasting porosity/density were sampled: low density/high porosity (Fig. 8c), intermediate density/medium porosity (Fig. 8d) and high density/low porosity Fig. 8e.

An increase in pore size is obvious after cycling, particularly within the intermediate and highly porous regions. As Table 1 shows, mean pore diameter increases markedly, most

notably in the most porous region of the as-sintered sample. Concurrently, the dense regions of the cycled specimen show a significantly lower level of porosity (6.8%), compared to the dense regions in the as-sintered specimen (35%). The percentage of porosity in the most porous regions, however, remains similar to its equivalent region in the as-sintered specimen, at around 41–42%. A few of these are crack-like, likely coalesced pores. It is interesting to note a large, near-vertically aligned pore/crack in the densest region of the cycled sample (Fig. 8e), although this feature was excluded from the pore analysis.

The formation of ellipsoidal isolated pores in the as-sintered condition is driven by the faster diffusion of vacancies at grain boundaries than within the grains. There are three atomic diffusion mechanisms active during sintering: surface, grain boundary and lattice diffusion. The generally higher levels of porosity observed in this work in comparison to others^{41–43} is attributable to the relatively low sintering temperature and time used, conditions under which surface diffusion takes precedence over lattice and grain boundary diffusion mechanisms.⁴⁴ The latter two processes are said to dominate at higher homologous temperatures and accelerate densification and pore shrinkage. Our earlier work confirms this, and found the amount of porosity to be determined by the sintering parameters, with lowest sintering pressures/temperatures and shortest sintering times resulting in the highest overall porosities.^{14,15}

Because of their larger radius of curvature, the vacancy concentration of larger pores is said to be lower than that of the smaller pores.⁴⁵ The tendency for the migration of vacancies from high to low concentration regions under temperature cycling, therefore, results in the annihilation of smaller pores in favour of larger ones, which resulted in the disappearance of numerous small pores and the growth of fewer larger pores. Thus, this manifests as increased mean pore diameter and reduced pore number. Same-sample 3D x-ray tomography analyses corroborate this, and showed that porous regions became more porous or developed into

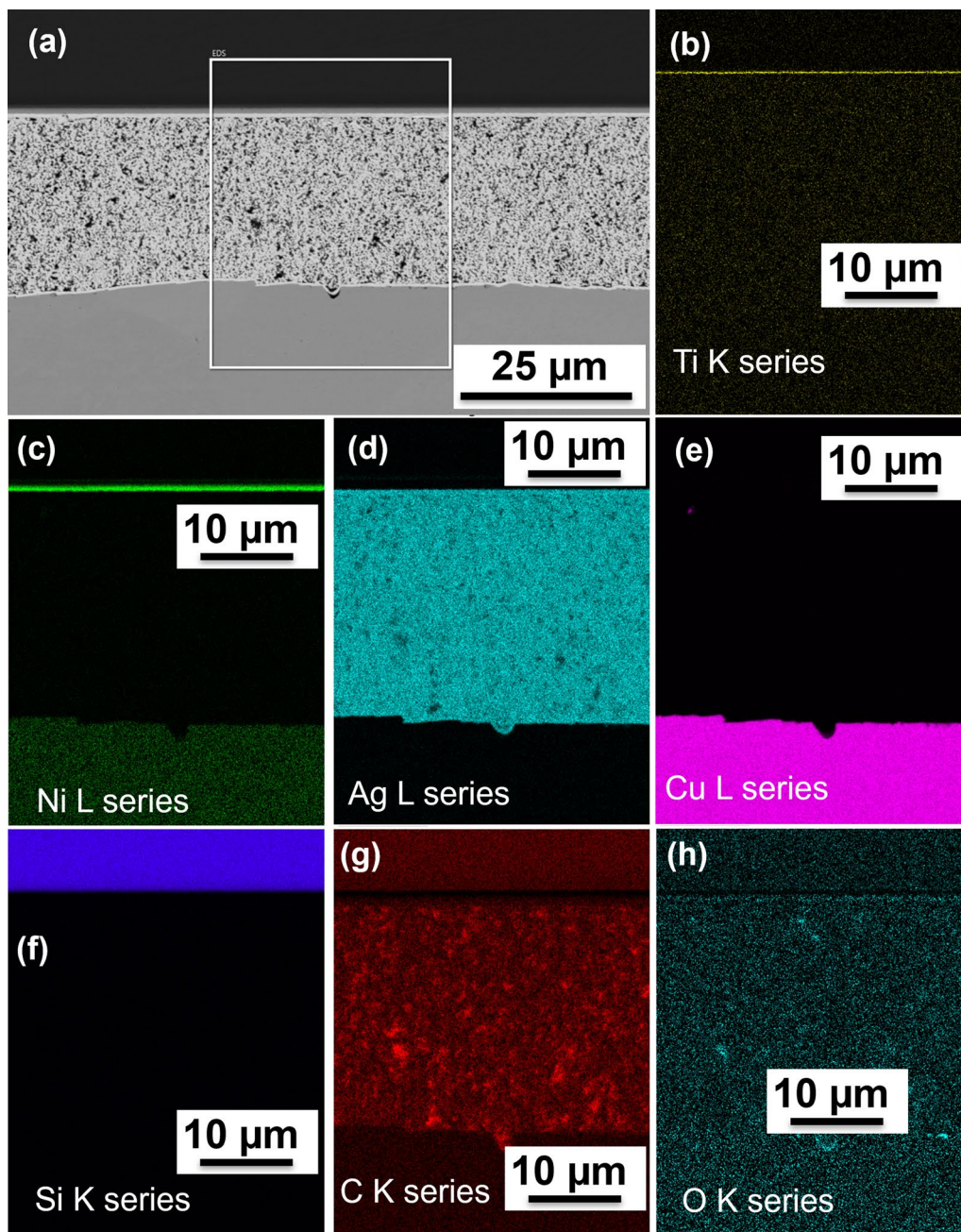


Fig. 6 (a) Electron backscatter image of the as-sintered bond showing the region selected for energy dispersive x-ray spectral (EDS) analysis. (b–h) Corresponding EDS images showing the spatial distributions of Ti, Ni, Ag, Cu, Si, C and O, respectively.

cracks during cycling, while contiguous regions became more dense.¹⁵

Grain Growth and Evolution of Grain Morphology and Textures of the Ag Layer

Both porous and dense regions of the as-sintered sample, as exemplified by their equivalent circle diameter or ECD (i.e., the diameter of a circle with the same area as the grain)

images and frequency plots (Figs. 9a, b and 10a), revealed very similar grain size distributions, consisting of fine grains averaging at approximately 216 nm and 237 nm, respectively (for an EBSD mapping step size of 50 nm), see Table II. The grain size achieved from sintering is said to be dependent on the duration of sintering, with finer grain sizes, associated with shorter total elapsed times from the onset of sintering.⁴⁵

For the power-cycled sample, EBSD imaging was performed on the three areas of contrasting porosity/density

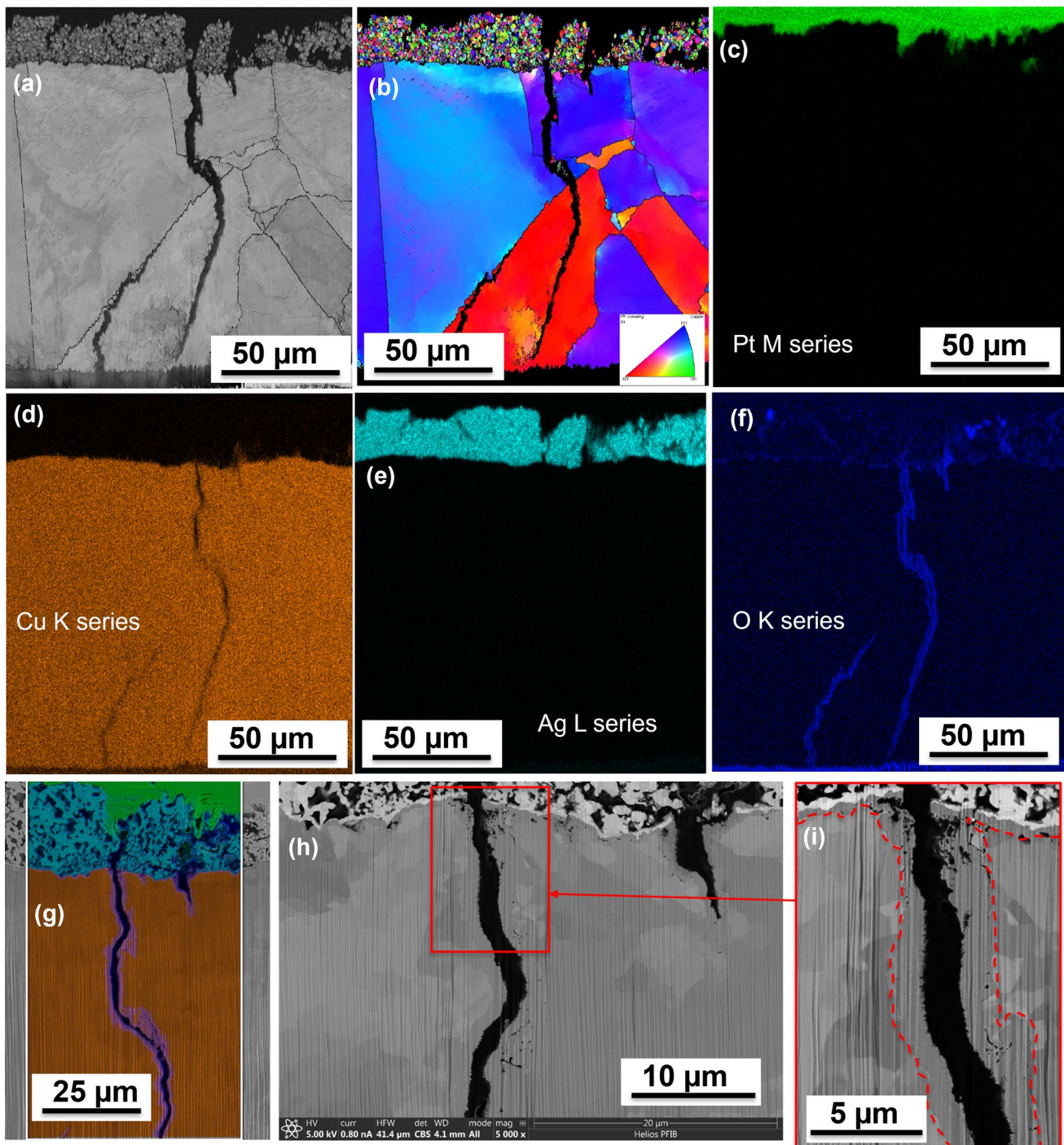


Fig. 7 Spectral analysis of Ag-Cu interface and cracks. (a) EBSD band contrast image and (b) corresponding EBSD IPF representation of the selected region, step size 0.2 μm. (c–f) EDS images showing

spatial distributions of Pt, Cu, Ag and O, respectively. (g) Layered EDS image, (h, i) backscattered electron image of the microstructure in the immediate vicinity of the crack.

shown previously in Fig. 8, using the same step size of 50 nm. The effect of subsequent temperature excursions during power cycling is clear. Figure 9c, d, and e show the spatial representations of ECD, and Fig. 10 is a box and whisker plot of grain size for different microstructural zones in the

two samples. When compared with the as-sintered sample, the cycled sample clearly shows significant grain growth in all zones, most appreciably in the high-density region. Grain size averages were estimated as 0.6 μm, 0.58 μm and 0.79 μm, respectively, for the high-porosity, intermediate

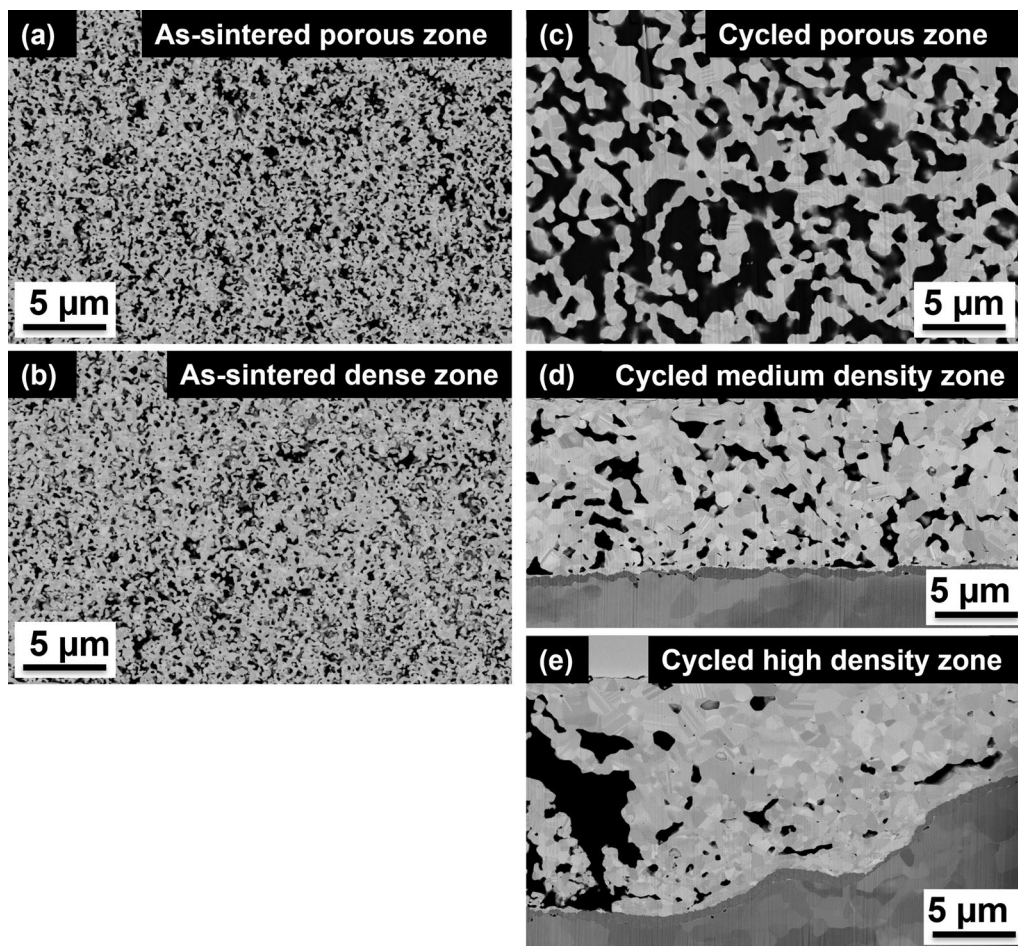


Fig. 8 Backscatter electron microstructures of (a) high-porosity and (b) high-density zones in the as-sintered sample, and (c) high-porosity, (d) intermediate-density and (e) high-density zones within the power-cycled sample.

and high-density regions (see Table II). In polycrystalline materials, grain growth is an expected outcome of exposure to ‘high’ temperature, even if anisothermal,⁴⁶ is driven by the achievement of a reduction in grain boundary interfacial energy⁴⁷ and occurs simultaneously as pore growth in sintered Ag attachments.⁴⁸

Unlike the as-sintered specimen, which shows relative uniformity of grain size with no apparent grain morphology variations in both its low- and high-density regions, there are clearly defined grain size gradients with respect to the through-thickness direction within the cycled specimen for the intermediate- and high-density sampling locations (Fig. 9d and e). These consist of a 200 nm ultrafine and uniform layer, about a grain in thickness, which can be seen nearest to the Cu substrate side. This layer of very fine grains may be Ni grains originating from the plating on the copper substrate, even though there was no obvious sign of Ni in the EDS visualisation (Fig. 7). Directly above this layer and near the interface with copper, a 4–5 μm thick band of fine, equiaxed grains can be seen. Further

towards the SiC end of the Ag-layer, there are significantly larger grains, with the high-density region showing the coarsest of these. The low-density, high-porosity region of the cycled sintered layer (Fig. 9c), on the other hand, exhibits a more uniformly distributed grain size along the attachment through-thickness, and consists of a mixture of fine and coarse grains with no apparent banding or layering as evident in the other two regions.

In Fig. 11, inverse pole figure (IPF) maps in the direction perpendicular to the sintering pressure, but parallel to predominant thermal cycling stresses are shown for both as-sintered and thermally cycled attachment layers. For both specimens and in all zones, grains appear randomly oriented. An exception is perhaps within the dense region of the thermally cycled specimen (Fig. 11e), in which two horizontal bands of small grains appear aligned parallel to $\langle 101 \rangle$ in the viewing direction parallel to thermal cycling stress; however, in general, there is no obvious spatial segregation of selected (the most prominent) ideal texture components.

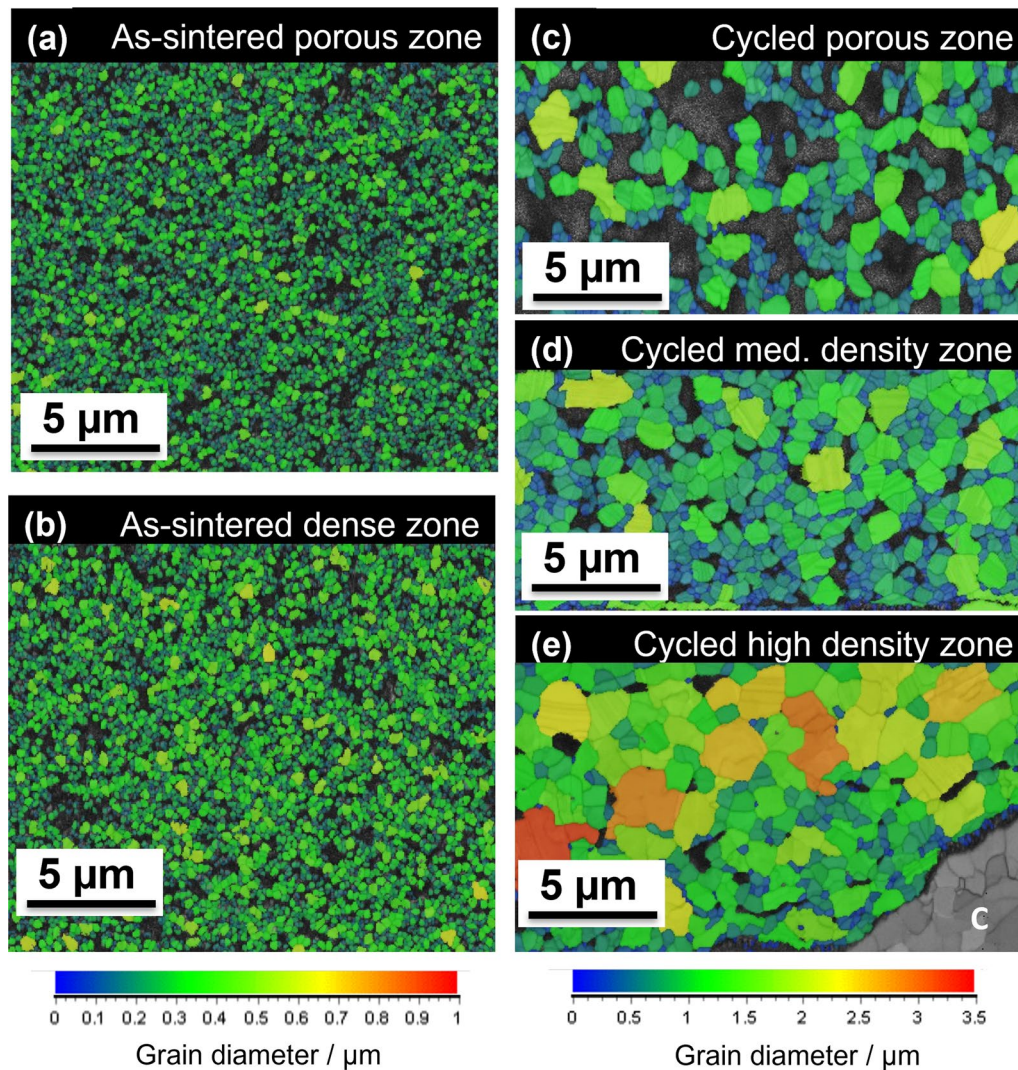


Fig. 9 EBSD equivalent circle diameter (ECD) representations of (a) high-porosity and (b) high-density zones in the as-sintered sample, and (c) high-porosity, (d) intermediate-density and (e) high-density zones within the power-cycled sample.

The absence of strong textures in the as-sintered sample is noteworthy. Stress–strain behaviour of sintered silver under monotonic uniaxial loading would suggest that strong deformation textures might have been expected within the Ag layer because of the high sintering pressures.⁴⁹ However, microstructural analyses of as-sintered Ag attachment structures in previous works^{23,50} did not show such highly deformed textures either. Furthermore, the predominance of randomly oriented, largely equiaxed ultrafine grains is perhaps indicative of the beginnings of microstructural restoration (specifically recrystallisation), during/post-sintering. Although there is less cold work when pressure and temperature are applied simultaneously during sintering than in succession,⁵¹ it is still expected that the large amount of grain boundary enthalpy stored in nanoparticles provides a significantly higher driving force

for grain growth processes than for bulk silver. For OFHC copper nanoparticles, for example, this is thought to be comparable to that of 100% cold worked bulk copper.⁵²

It is also interesting to note the different extents to which the two specimens exhibit CSL boundaries, and how this varies for regions differing in density/porosity. The occurrence of nanoscale twins in sintered attachments has been reported by Wang et al.²⁸ and Yang et al.³⁶ and is observable in Choe et al.'s work.⁴⁸ In the present work, annealing twins are found in both as-sintered and cycled specimens and in all density regions to varying degrees in the IPF maps in Fig. 11. For the as-sintered specimen, these nanoscale twins are more easily seen in IPF maps acquired using a smaller step size (20 nm), more appropriate considering its fine-grained structure. These are presented in Fig. 12.

In both as-sintered and power-cycled specimens, the band contrast images (Fig. 13) show that twins make up the vast majority of the low angle grain boundaries in all both porous and dense regions. The boundary images in Fig. 14 confirm that these are predominantly the Σ3 type with a 60° misorientation angle. In the as-sintered specimen, twin boundaries appear relatively uniformly distributed across the through-thickness of the attachment in both porous and dense regions, with a slightly increased twin density in the more porous sampling region (51% versus 42% imaged using a 20 nm step size). However, in the power-cycled specimen, there are clear differences in both twin density and in how these CSL boundaries are spatially distributed in the porous and dense regions. Twins are most prevalent near the copper boundary in the dense sampling location, while they appear widespread and uniformly distributed within the porous region. Furthermore, there are significantly fewer twins in the coarse-grained part of the dense region, with a twin density of 23%, compared to 42% in the high-porosity sampling location (see Table II).

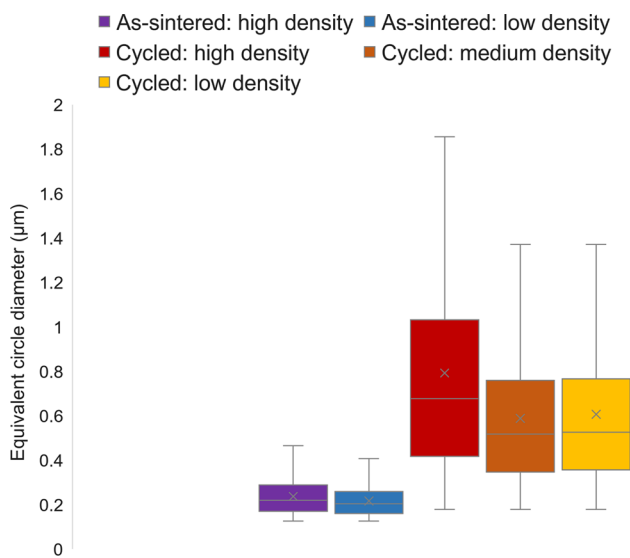


Fig. 10 Box and whisker plot of the estimated grain diameter of different microstructural zones within the as-sintered and power-cycled samples (Color figure online).

The formation of twins in fcc metals requires significant deformation stresses⁵³ and is indicative of dynamic recrystallisation.⁴⁷ In the as-sintered specimen, cold work under compressive stress associated with sintering creates conditions favourable for the formation of annealing twins, as expected in fcc materials with low stacking fault energy. Another factor facilitating twin formation maybe the localised high levels of accumulated plastic strain at the Ag-SiC interface due to their mismatched coefficients of thermal expansion (CTE) under thermal fluctuations (these are 4.1, 19.4 and $17.5 \times 10^{-6} \text{ K}^{-1}$, respectively, for SiC, sintered Ag and Cu^{54,55}). This may explain their spatial non-uniformity within the dense region of the cycled specimen, that is, their concentration near the material Ag-SiC interface (as opposed to the Ag-Cu Interface) where the CTE mismatch is smaller. However, if the deformation stress approaches or exceeds a certain critical level, twin formation can be bypassed in favour of recrystallisation and nucleation of fine grains. Unlike twin boundaries, which are less likely to migrate under high temperatures⁵³ and current stress^{1-4,56} due to their low energy, the newly formed fine grains readily coarsen under thermal cycling.

These elements may help to explain the varying microstructures observed relative to porosity. As previously mentioned, the differing densities are thought to arise from localised height differences at a fine scale on the copper substrate which produce locally varying sintering pressures. In the as-sintered specimen, the sampled high- and low-density regions were similar in layer thickness at around 25–26 µm. Within the cycled sample, the thickness of the sintered layer in the low-density/high-porosity sampling region (35 µm) is considerably greater than the high-density/low-porosity region (approximately 6 µm at its narrowest point). The high density here is most likely due to the bulge on the copper surface (seen as the upward curvature), which resulted in a higher-than-average sintering pressure locally. It is likely that, as explained above, the sintering pressure in high-density regions is high enough to result in the prevention/reduction of twin formation, in favour of newly nucleated grains with highly mobile boundaries from the start. As heterogeneous porosities inevitably result in localised variations in

Table II Grain size estimations of the as-sintered and power-cycled samples

Average values	As-sintered (20 nm step size)		As-sintered (50 nm step size)		After power cycling (50 nm step size)		
	Porous region	Dense region	Porous region	Dense region	Low density	Medium density	High density
Grain diameter (µm)	0.173	0.186	0.216	0.237	0.60	0.58	0.79
Grain count	615	534	5680	5114	1150	1094	329
Twin density (%)	51	42	28	28	42	39	23

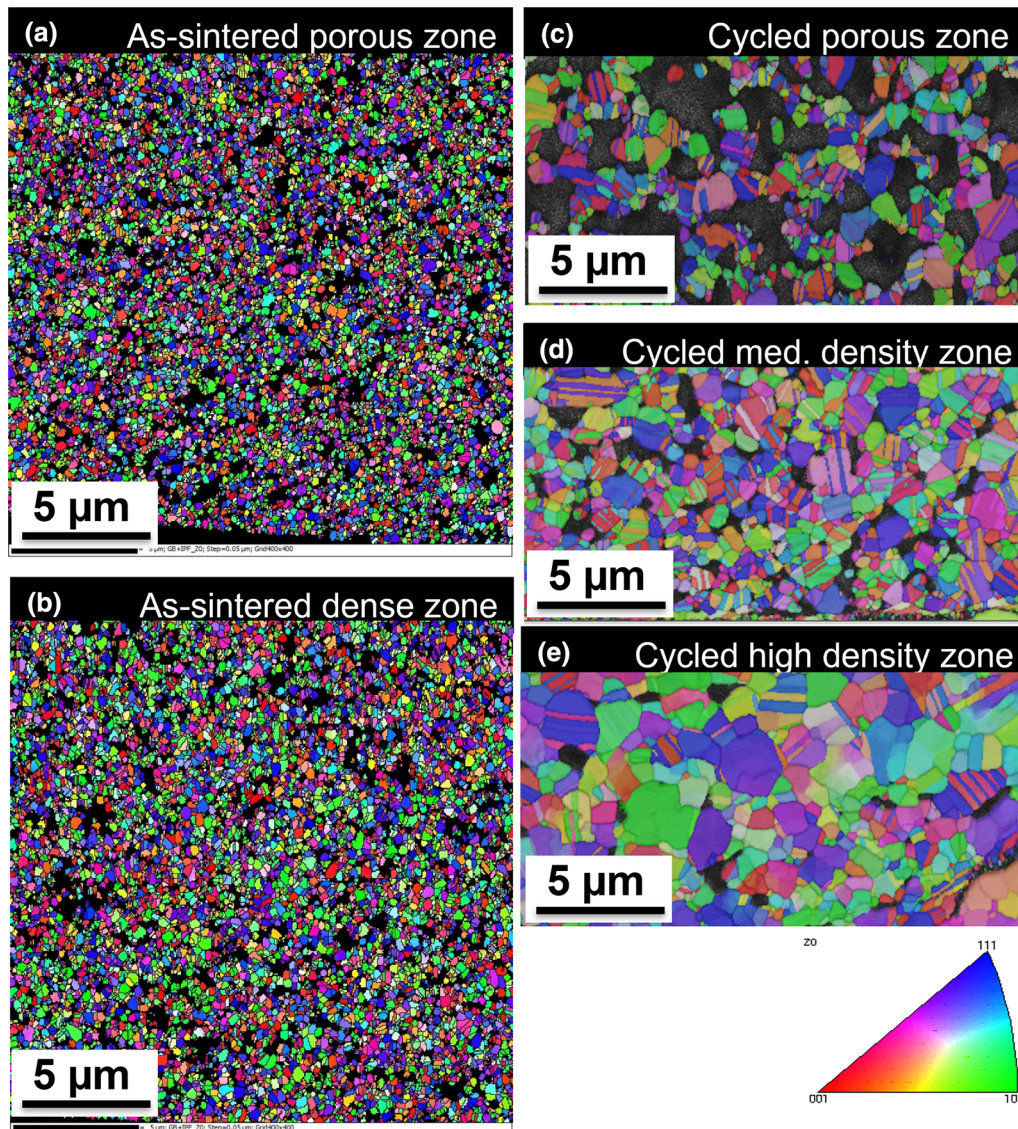


Fig. 11 EBSD inverse pole figure (IPF) representations obtained using a step-size of 50 nm of the (a) high-porosity and (b) high-density zones in the as-sintered sample, and (c) high-porosity and (d) intermediate-density and (e) high-density zones within the power-cycled sample

electrical and thermal conductivity, variation in degree of microstructural restoration can also be expected. It is also plausible that in high density regions, increased contact area between grains creates the path of least resistance for the flow of current and heat through the sintered nanoAg layer to the other elements of the package. Thermal energy and electrical current provide activation and driving force for dislocations mobility and atoms migration across grain boundaries, resulting in Ostwald ripening,⁴⁷ and eventually

fewer, larger and randomly oriented grains. The spatial segregation of grain size observable is suggestive of a continuing trade-off between recovery, recrystallisation and grain growth on one hand, and on the other hand, a localised accumulation of dislocations at the Ag-Cu and Ag-SiC boundaries due to increased viscoplastic strains, and the formation of bands or strips of high twin density zones close to the abovementioned boundaries.

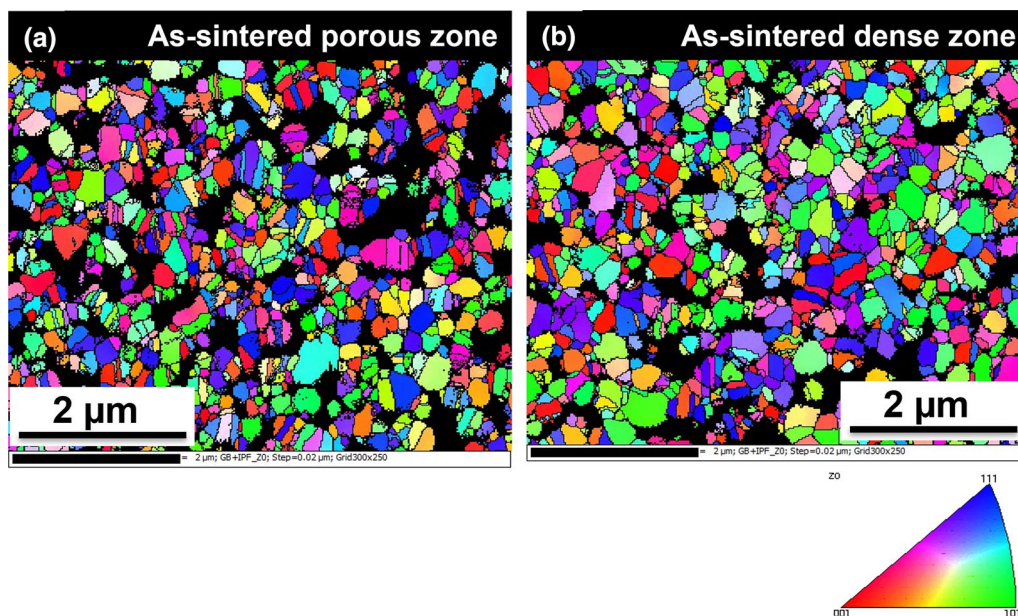


Fig. 12 EBSD inverse pole figure (IPF) representations obtained using a step size of 20 nm of the (a) high-porosity and (b) high-density zones in the as-sintered sample.

Conversely, the presence of numerous or large pores may be expected to obstruct the flow and supply of thermal and electrical energy to grains in the said regions. Pores and discontinuities may also create natural barriers which may function to impinge or disrupt the above diffusion-driven processes. These factors, together with the high prevalence of twins which are inherently resistant to dislocation creep,⁵³ act together to restrict grain growth.

Crack Initiation, Propagation and Transitioning Across the Ag-Cu Boundary into the Cu Layer

Segmentation and three-dimensional rendering of the reconstructed FIB serial sectioning dataset obtained from the cycled specimen (as described in section 2.4.2) provides illustrations which allow us to make some important observations. Firstly, it allows us to digitally ‘strip’ the Ag layer away from the copper substrate. In Fig. 15, a series of still images show this progressive unpeeling and exposes new fine-scale detail of the copper surface. Some, but not all, of the vertically aligned coalesced pores/cracks can be seen to follow what look like grain boundary contours, i.e., the boundaries between high and low topographies. A nascent crack network which is still fully contained within the sintered layer and has not yet made contact with the copper

surface (circled in Fig. 15c) also sits directly above and mirrors the outline of a grain boundary several microns beneath it. This suggests that the cracks may originate near the top (SiC) end of the sintered layer and progress towards the copper end with increasing number of cycles, perhaps because the mismatch in coefficient of thermal expansion between SiC and Ag is greater than between Cu and Ag.^{54,55} Previous work demonstrates that these cracks, which initiated and/or developed from within high-porosity regions, did not tend to propagate laterally in the first instance, but occurred preferentially in relatively narrow, vertical columns, often directly above grain boundaries on the surface of the copper substrate.^{14,15} This agrees with other researchers,^{55–58} and is thought to be explained by in-plane macroscopic tensile strains.⁵⁸

When the Ag layer is completely stripped off (Fig. 15e), the entirety of the surface and topography of the copper substrate beneath is revealed. This shows the typical peaks and troughs responsible for the non-uniform sintering pressure profile across the attachment. Even though some degree of substrate roughness is desirable for mechanical integrity,⁵⁹ pronounced variability of topography creates pronounced localised porosity variability, and consequently heterogeneous microstructural development under thermomechanical loading.

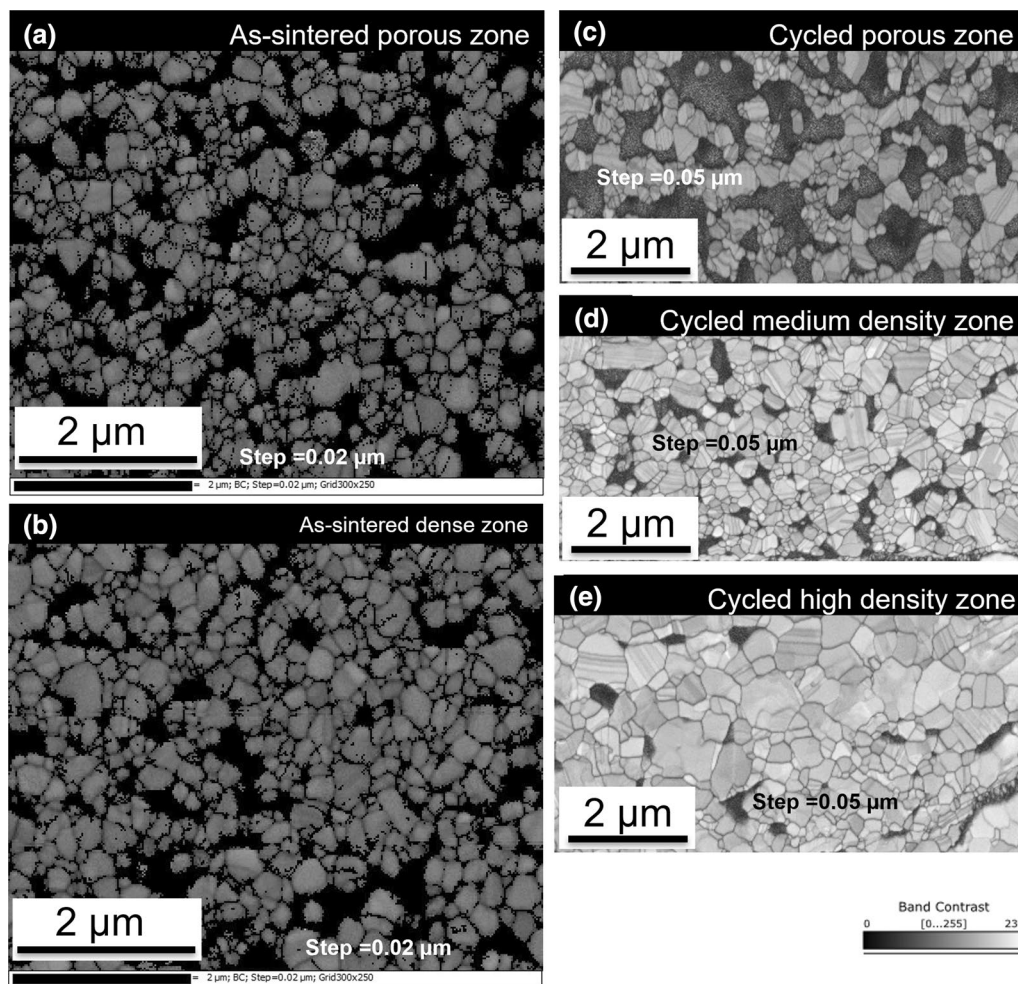


Fig. 13 EBSD band contrast (BC) representations of the (a) high-porosity and (b) high-density zones in the as-sintered sample, and (c) high-porosity and (d) intermediate-density and (e) high-density zones within the power-cycled sample.

A similar 3D reconstruction of the FIB serial sectioning dataset of secondary electron images for the cycled specimen (as described in section 2.4.2) allows a series of two-dimensional lateral cross-sections of the Ag and copper layers to be obtained (see Fig. 16). These cross-sections (slices *a* to *e*) have been taken at different depths through the Ag and copper layers and provide a fine-scale, correlative view of the heterogeneous pore structure and its relationship to the global microstructure of the Ag layer, as well as the morphology of the copper beneath. They also reveal the microstructural contexts for the cracks within the copper. For ease of reference, a few features of interest are labelled 1–6, and their evolution is tracked through progressive lateral sections *a* to *e*. The cracks near 1 and 5 appear widest near the top (SiC end) of the Ag layer, and taper in width as we move

from *a* to *e*. Within the copper layer, very small subgrains/dislocation cells can be seen adjoining major cracks on both sides. The cracks visible in slice *e* do not appear to fall on major grain boundaries.

Microstructural Observations of the Copper Substrate

The (large) grain size and extensive crack lengths within the Cu layer necessitate a large-area EBSD examination in order to fully understand the crack-structure relationships. Figures 17 and 18 show visual representations of ECD and IPF orientation maps in the X and Z viewing directions for the as-sintered and cycled specimens obtained using a step size of 0.5 μm and covering an area of 2.3 mm \times 0.3 mm.

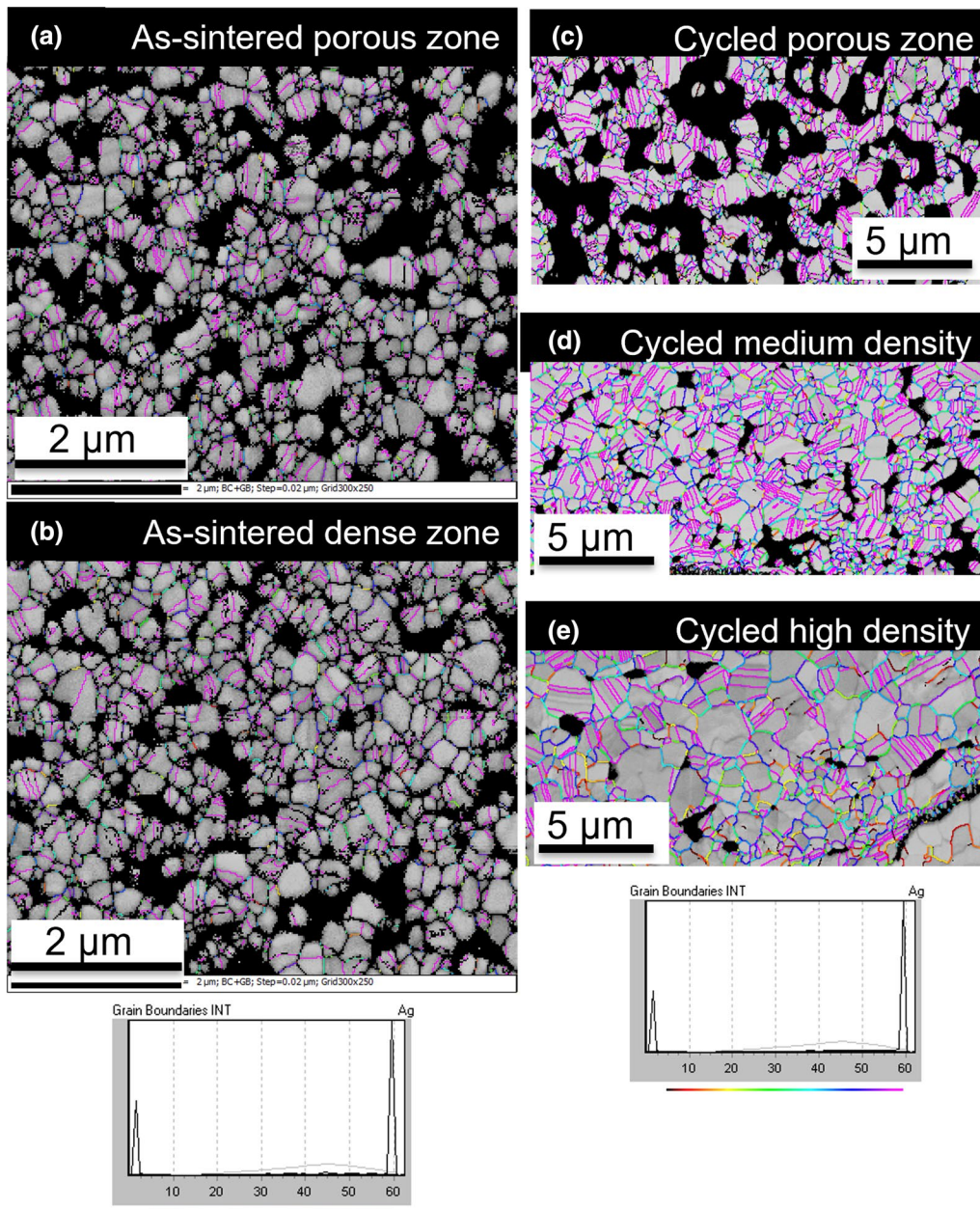


Fig. 14 EBSD grain boundary maps of the (a) high-porosity and (b) high-density zones in the as-sintered sample, and (c) high-porosity and (d) intermediate-density and (e) high-density zones within the

power-cycled sample, showing high misorientation ($\Sigma 3$ twin) boundaries in pink (Color figure online).

On observing and comparing the ECD images in Figs. 17c and 18c, some grain refinement after cycling is evident. This is confirmed by grain diameter estimations obtained using the linear intercept method, which show the as-sintered and power-cycled specimen grain sizes to be 66.3 μm and

50.6 μm, respectively (see Table II). It is worth noting that the large step size may have resulted in fine-grained regions being unresolved and thus excluded from this estimation.

The grains within the copper substrates both prior to and after power cycling are clearly significantly larger than in

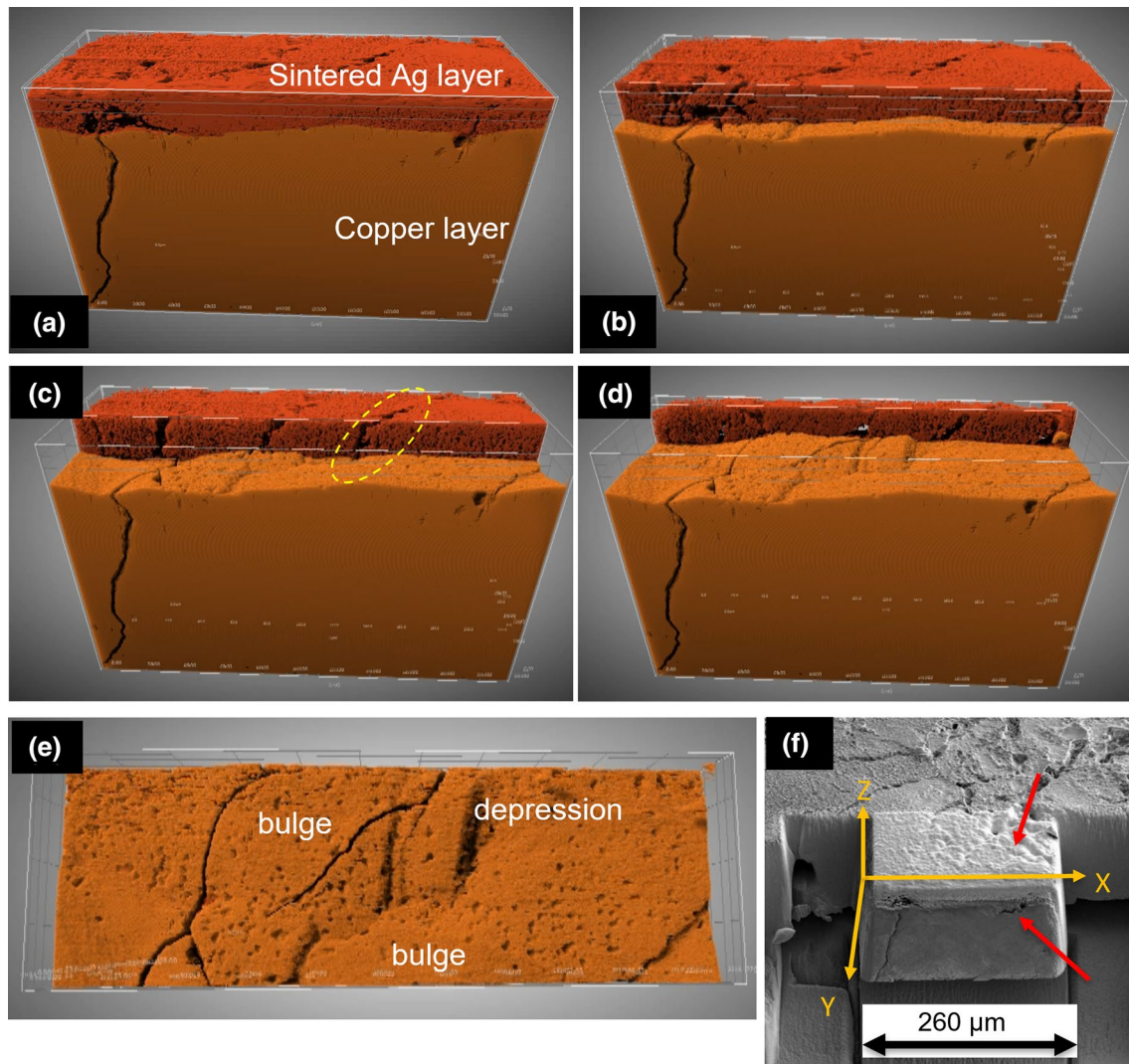


Fig. 15 (a–d) 3D renderings of showing progressive stripping off of the sintered Ag layer to reveal copper surface. (e) Completely exposed copper surface. (f) Overview of sampling and p-FIB serial sectioning location.

the Ag layer and also appear randomly oriented. The IPF images show annealing twins in both samples, but a few deformation twins are also noticeable within the cycled sample (Fig. 18d and e). Considering that the axis of alternating compressive and tensile forces which act on the copper layer during cycling are overwhelmingly in the lateral planes,^{56,58} it is interesting to observe several twin grains aligned with $\langle 111 \rangle$ when viewed in X and Y directions within the cycled sample. The field of view contains three major cracks emanating from low-porosity regions within the sintered layer (see Fig. 18a). Although the crack paths at the Ag-Cu interface appear controlled by the major grain boundaries on the copper surface, this seems to alter within the copper bulk.

All three major cracks propagate through the Cu substrate transgranularly (the grains on adjoining sides of the cracks can be seen to possess the same orientation), with very little tortuosity observable at a few, short intergranular propagation segments. This is indicative of crack instability due to a high stress-intensity factor⁶⁰ and is not uncommon under cyclical loading⁶¹ (for clarity, an enlarged view of the crack labelled (I) in Fig. 18 is presented in Fig. 19). It is also interesting to observe smaller grains closest to the propagating cracks, a few of which contain deformation twins.

The annealing twins are mostly contained within large parent grains in both specimens, and in the cycled specimen, these large grains appear some distance from the

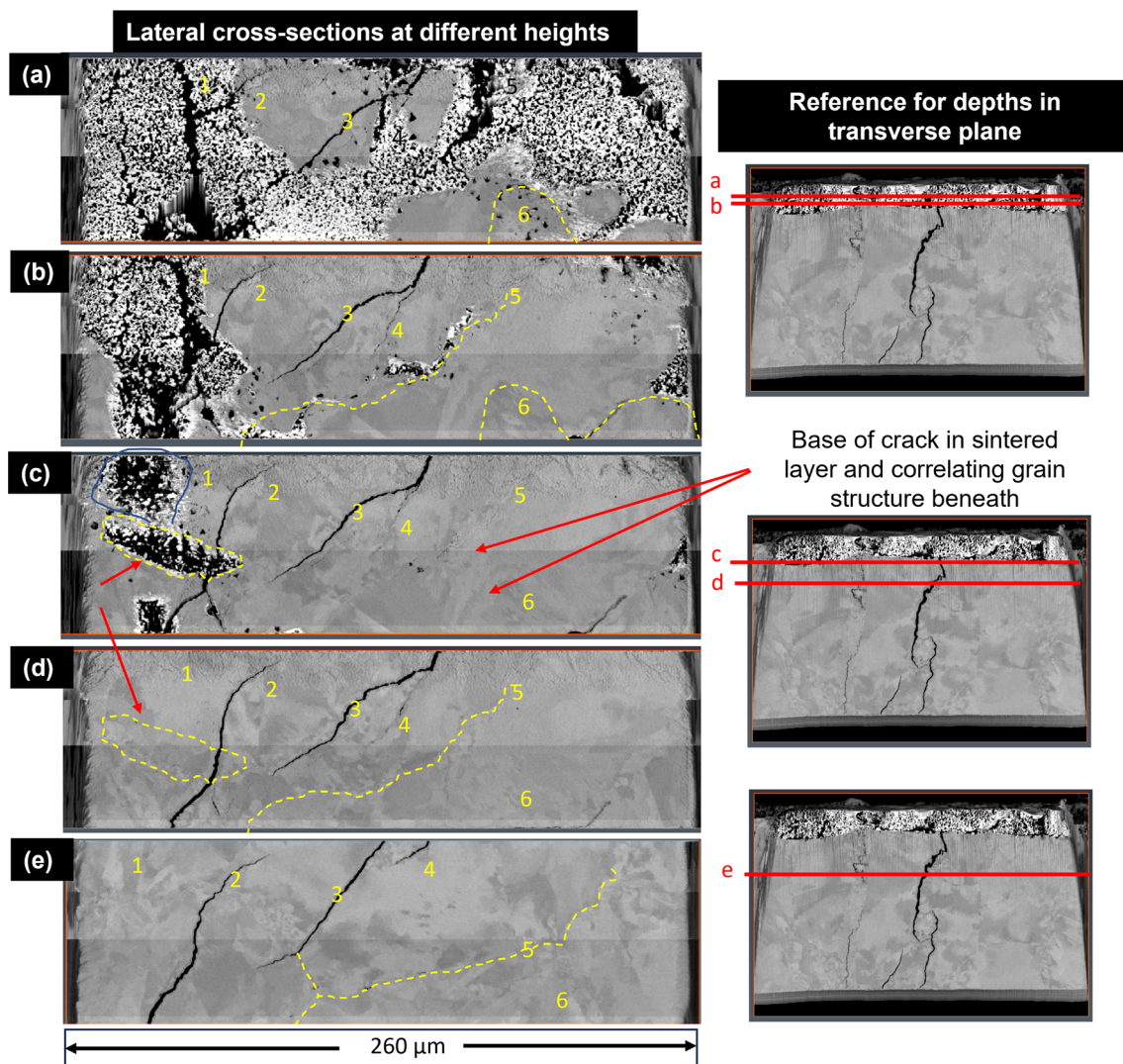


Fig. 16 Reconstructed 3D FIB serial sectioning dataset of secondary electron images for the cycled specimen: progressive virtual slices (a–e) taken at different depths through the Ag and Cu layers.

propagating cracks. It can be recalled from Fig. 16 that high dislocation densities (subgrains/cells) flank transgranular cracks visible in the lateral plane of the copper layer on both sides, suggestive of strain localisation at the crack front and a continuous presentation of slip planes at weak angles in the propagation direction. This is further exemplified by the corresponding backscatter image in Fig. 19c, which shows numerous subgrains/cells adjacent the crack (see arrows). This is also evidenced by darker pixels close to the crack tip in the band contrast image in Fig. 19b.

Summary and Conclusions

Porosity is an unavoidable outcome of the sintering process, occurring to a greater or lesser extent depending on sintering parameters and substrate properties.^{12,13} In this paper, we have attempted to explore the fine-scale microstructural features of this porosity, and understand how it functions within sintered attachments in a reliability context. This has been achieved by combining temporal data obtained at the meso-length scale using 3D x-ray tomography, with subsequent subsampling via FIB/EBS to probe nanoscale microstructural features. We have attempted to understand

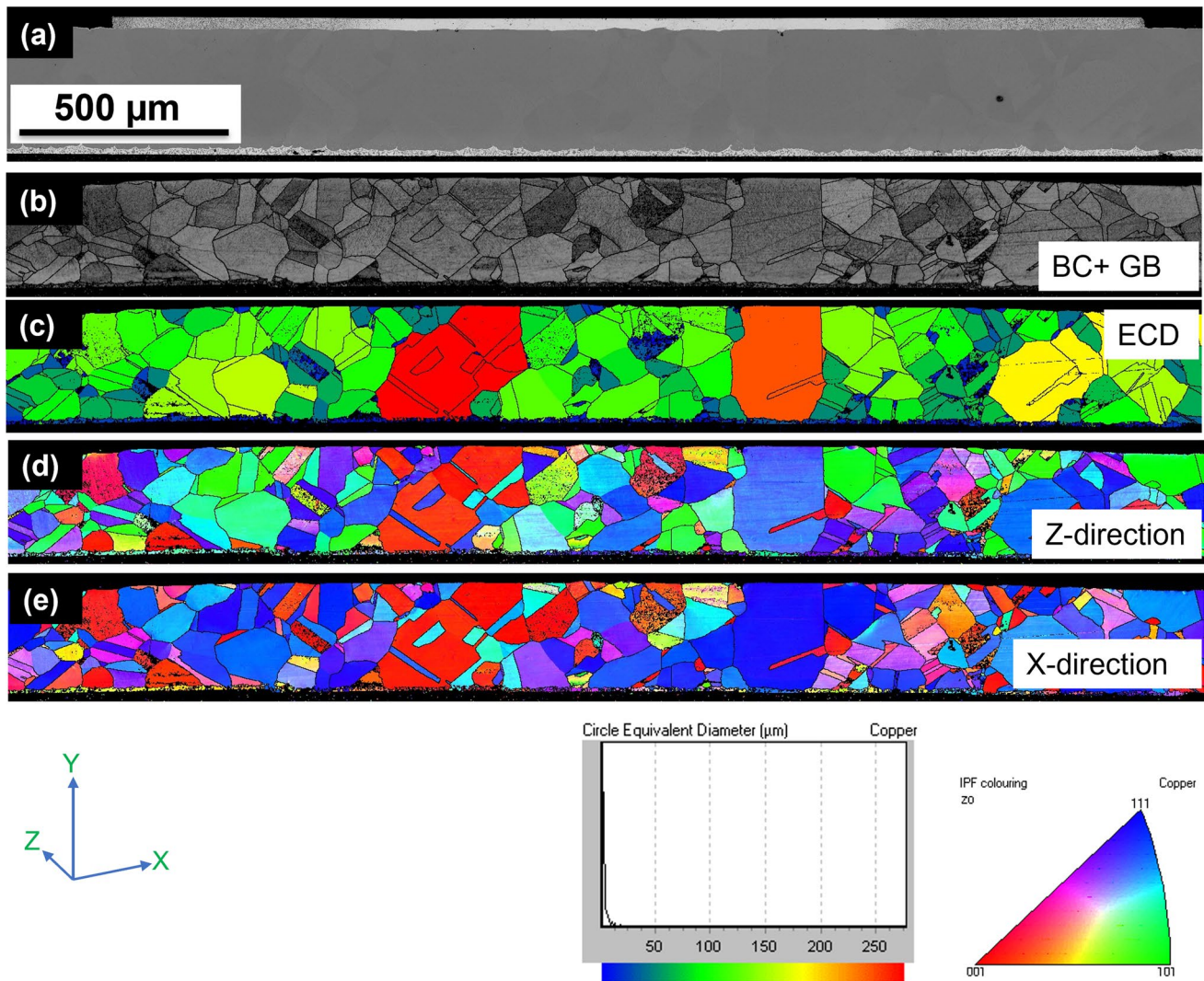


Fig. 17 (a) Backscatter image and (b–e) corresponding EBSD images for the as-sintered sample obtained using a step size of $0.5\ \mu\text{m}$, (b) equivalent circle diameter (ECD) representation, (c, d) inverse pole figure (IPF) maps in the Z and X viewing directions, respectively.

the relationship between porosity and grain structure by sampling specimens to look at regions of contrasting densities. In so doing, we see that in the as-sintered condition, the attachment has a heterogeneous nanoscale grain structure with an interspersion of nanoscale pores. Microstructural transformation occurs non-uniformly across the joint under power cycling, evidently influenced by ab initio densities and also by thermomechanical stresses localised at the interface between Ag and Cu. Significant grain growth is noticeable, most pronounced in the densest of regions, and attributed to more paths available for species and dislocation transport. Both as-sintered and extensively cycled conditions exhibit a high proportion of $\Sigma 3$ -type grain boundaries, the densities of which appear to reduce post-cycling, particularly

in the least porous regions. More porous regions retain more twin boundaries than denser regions. The significance of this in terms of localised stress response under cycling should be ascertained. It is also interesting to observe significant increase in pore diameter due to growth and/coalescence of isolated pores in more porous regions. The surface topology of the copper substrate appears to influence the spatial distribution of pores. Although cracks are initially observed within the sintered joint, and subsequently appear to traverse the Ag-Cu-interface into the Cu substrate, further work is required to clarify the role of the substrate in their initiation and propagation within the Ag layer.

A broader discussion is also required to consider and separate out the gross effects of the heterogeneous pore

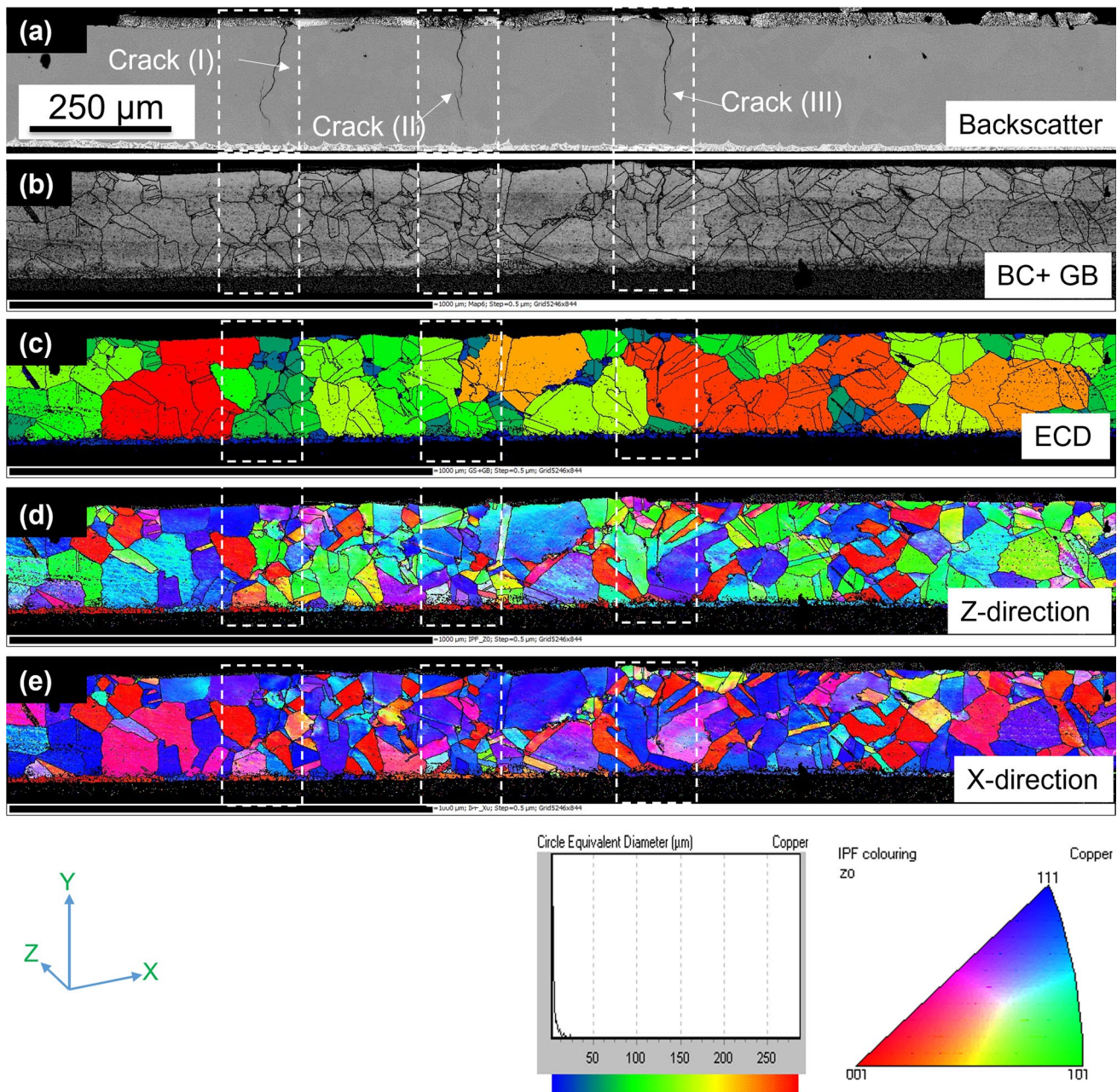


Fig. 18 Backscatter image and (b–e) corresponding EBSD images for the power-cycled sample obtained using a step size of 0.5 μm, (b) equivalent circle diameter (ECD) representation, (c, d) inverse pole figure (IPF) maps in the Z and X viewing directions, respectively.

structure. Local variations in thermal conductivity can be expected. Additionally, there may be increased compliance which may be advantageous in terms of the plastic strain response of the attachment, at system level. The tendency of pores to coalesce to form vertically aligned discontinuities may also create an anisotropic stress response which

may be advantageous against lateral shear stresses. Future work will systematically examine these hypotheses. Finally, other wider implications of short sintering times, such as potentially more challenging process control on a commercial scale (e.g., reproducibility and yield) also require further investigation.

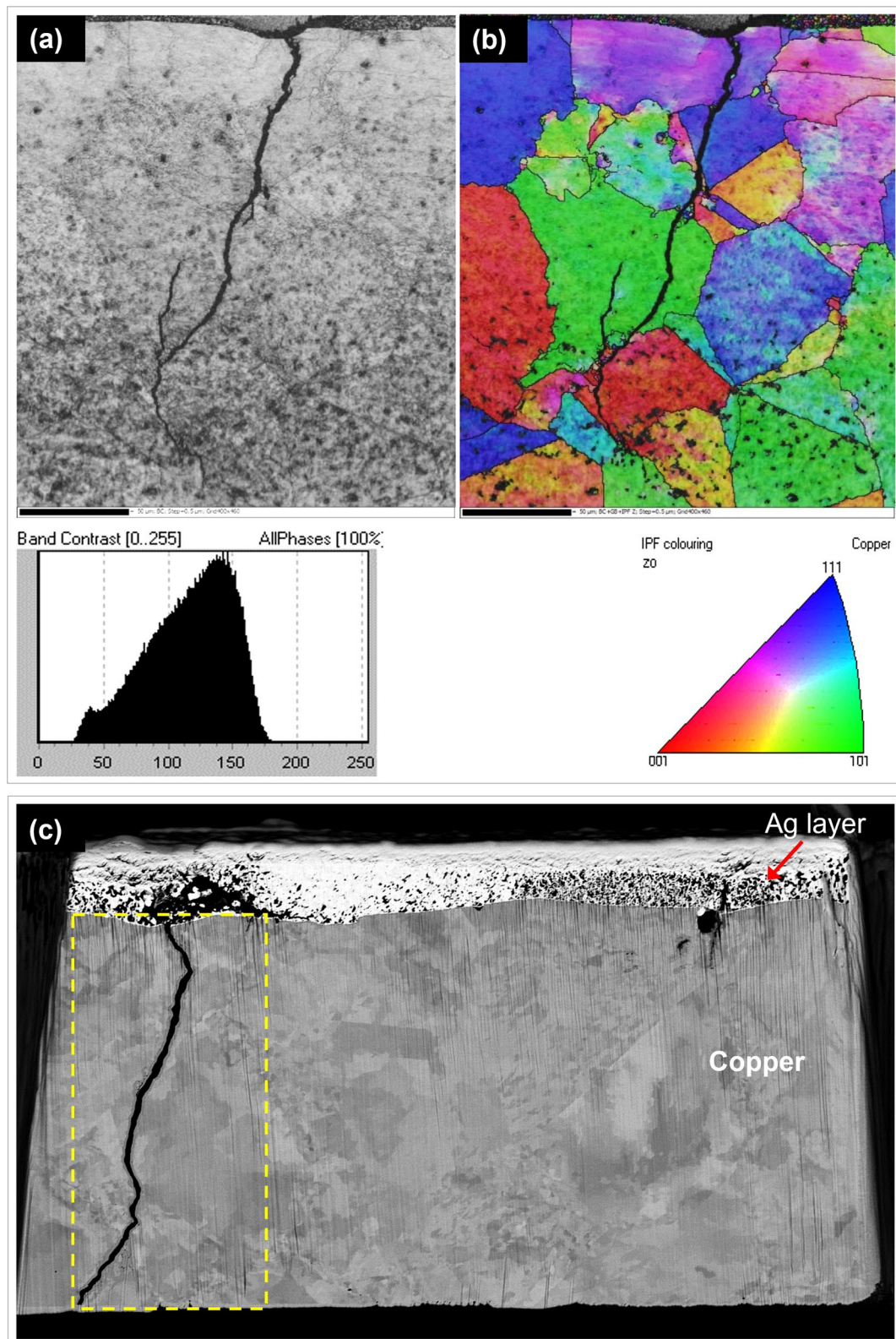


Fig. 19 Enlarged view of the crack labelled (I) in Fig. 18: (a) band contrast and (b) inverse pole figure (IPF) map in the Z viewing direction; (c) corresponding slice from reconstructed 3D FIB serial sectioning dataset.

Acknowledgments We are grateful to the Loughborough Materials Characterisation Centre for equipment access and support and including access to the Helios PFIB, funded by the EPSRC grant EP/P030599/1. We also thank Oscar Khaselev and Mike Marczl of Cookson Electronics for providing Ag nanoparticle paste. We sincerely thank the Oxford Micromechanics Group for an interesting discussion which has stimulated ideas for future work. This work was supported by Mentor Graphics and the UK Engineering and Physical Sciences Research Council projects EP/K035304/1, EP/R004366/1 & EP/R004501/1 through the Centre for Power Electronics and the EU Commission's 7th Framework Programme Cleansky2 JU EMINEO.

Conflict of interest The authors declare that they have no conflict of interest.

Open Access This article is licensed under a Creative Commons Attribution 4.0 International License, which permits use, sharing, adaptation, distribution and reproduction in any medium or format, as long as you give appropriate credit to the original author(s) and the source, provide a link to the Creative Commons licence, and indicate if changes were made. The images or other third party material in this article are included in the article's Creative Commons licence, unless indicated otherwise in a credit line to the material. If material is not included in the article's Creative Commons licence and your intended use is not permitted by statutory regulation or exceeds the permitted use, you will need to obtain permission directly from the copyright holder. To view a copy of this licence, visit <http://creativecommons.org/licenses/by/4.0/>.

References

1. L. Menager, C. Martin, B. Allard, and V. Bley, Industrial and lab-scale power module technologies: a review, IECON 2006—32nd Annual Conference on IEEE Industrial Electronics, Paris, France, pp. 2426–2431 (2006).
2. S. Ramminger, P. Türkes, and G. Wachutka, Crack mechanism in wire bonding joints. *Microelectron. Reliab.* 38(6–8), 1301 (1998).
3. I. Lum, M. Mayer, and Y. Zhou, Footprint study of ultrasonic wedge-bonding with aluminum wire on copper substrate. *J. Electron. Mater.* 35, 433 (2006).
4. H. Niu, A review of power cycle driven fatigue, aging, and failure modes for semiconductor power modules, 2017 IEEE International Electric Machines and Drives Conference (IEMDC), Miami, FL, USA, pp. 1–8 (2017).
5. W.J. Plumbridge and C.R. Gagg, The mechanical properties of lead-containing and lead-free solders—meeting the environmental challenge. *Proc. Inst. Mech. Eng. Part L J. Mater. Des. Appl.* 214(3), 153 (2000).
6. M. Knoerr, S. Kraft, and A. Schletz, Reliability assessment of sintered nano-silver die attachment for power semiconductors, 2010 12th Electronics Packaging Technology Conference, Singapore, 2010, pp. 56–61 (2010).
7. I.L. Regalado, J.J. Williams, S. Joshi, E.M. Dede, Y. Liu, and N. Chawla, X-ray microtomography of thermal cycling damage in sintered nano-silver solder joints. *Adv. Eng. Mater.* 21, 1801029 (2019).
8. K.S. Siow, Mechanical properties of nano-silver joints as die attach materials. *J. Alloys Compd.* 514, 6 (2012).
9. S. Soichi and K. Sukanuma, Low-temperature and low-pressure die bonding using thin Ag-flake and Ag-particle pastes for power devices. *IEEE Trans. Compon. Packag. Manuf. Technol.* 3(6), 923 (2013).
10. H. Alarifi, A. Hu, M. Yavuz, and Y.N. Zhou, Silver nanoparticle paste for low-temperature bonding of copper. *J. Electron. Mater.* 40, 1394 (2011).
11. Y. Su, G. Fu, C. Liu, K. Zhang, L. Zhao, C. Liu, A. Liu, and J. Song, Thermo-elasto-plastic phase-field modelling of mechanical behaviours of sintered nano-silver with randomly distributed micro-pores. *Comput. Methods Appl. Mech. Eng.* 378, 113729 (2021).
12. G.F. Bocchini, The influences of porosity on the characteristics of sintered materials. *SAE Trans.* 95, 790 (1986).
13. F. Ternero, L.G. Rosa, P. Urban, J.M. Montes, and F.G. Cuevas, Influence of the total porosity on the properties of sintered materials—a review. *Metals* 11(5), 730 (2021).
14. J. Dai, J. Li, P. Agyakwa, M. Corfield, and C.M. Johnson, Comparative thermal and structural characterization of sintered nano-silver and high-lead solder die attachments during power cycling. *IEEE Trans. Device Mater. Reliab.* 18, 256 (2018).
15. P. Agyakwa, J. Dai, J. Li, B. Mouawad, L. Yang, M. Corfield, and C.M. Johnson, Three-dimensional damage morphologies of thermomechanically deformed sintered nanosilver die attachments for power electronics modules. *J. Microsc.* 277, 140 (2020).
16. J.G. Bai, Z.Z. Zhang, J.N. Calata, and G.Q. Lu, Low-temperature sintered nanoscale silver as a novel semiconductor device-metallized substrate interconnect material. *IEEE Trans. Compon. Packag. Manuf. Technol.* 29, 589 (2006).
17. W. Guo, G. Fu, B. Wan, and M. Zhu, Reconstruction of pressureless sintered micron silver joints and simulation analysis of elasticity degradation in deep space environment. *Appl. Sci.* 10(18), 6368 (2020).
18. R. Kimura, Y. Kariya, N. Mizumura, and K. Sasaki, Effect of sintering temperature on fatigue crack propagation rate of sintered Ag nanoparticles. *Mater. Trans.* 59(4), 612 (2018).
19. P. Gadaud, V. Caccuri, D. Bertheau, J. Carr, and X. Milhet, Ageing sintered silver: relationship between tensile behavior, mechanical properties and the nanoporous structure evolution. *Mater. Sci. Eng. A* 669, 379 (2016).
20. K. Wakamoto, Y. Mochizuki, T. Otsuka, K. Nakahara, and T. Namazu, Tensile mechanical properties of sintered porous silver films and their dependence on porosity. *Jpn. J. Appl. Phys.* 58, SDDL08 (2019).
21. M. Wang, Y.H. Mei, J. Jin, S. Chen, X. Li, and G.Q. Lu, Pressureless sintered-silver die-attach at 180C for power electronic packaging. *IEEE Trans. Power Electron.* 6(11), 12141 (2021).
22. F. Qin, Y. Hu, Y. Dai, T. An, and P. Chen, Evaluation of thermal conductivity for sintered silver considering aging effect with microstructure based model. *Microelectron. Reliab.* 108, 113633 (2020).
23. C. Chen, Z. Zhang, D. Kim, T. Sasamura, Y. Oda, M.C. Hsieh, A. Iwaki, A. Suetake, and K. Sukanuma, Interface reaction and evolution of micron-sized Ag particles paste joining on electroless Ni-/Pd-/Au-finished DBA and DBC substrates during extreme thermal shock test. *J. Alloys Compd.* 862, 158596 (2021).
24. Z.Z. Fang and H. Wang, Densification and grain growth during sintering of nanosized particles. *Int. Mater. Rev.* 53, 326 (2008).
25. J. Li, I. Yaqub, M. Corfield, P. Agyakwa, and C. M. Johnson, Comparison of thermo-mechanical reliability of high-temperature bonding materials for attachment of SiC devices, CIPS 2014; 8th International Conference on Integrated Power Electronics Systems, Nuremberg, Germany, 2014, pp. 1–7, (2014).
26. Y. Lu, S. Liu, L. Weng, Z. Li, and L. Xu, Fractal analysis of cracking in a clayey soil under freeze–thaw cycles. *Eng. Geol.* 208, 93 (2016).
27. J. Yan, G. Zou, A. Wu, J. Ren, J. Yan, A. Hu, and Y. Zhou, Pressureless bonding process using Ag nanoparticle paste for flexible electronics packaging. *Scr. Mater.* 66(8), 582 (2012).
28. S. Wang, M. Li, H. Ji, and C. Wang, Rapid pressureless low-temperature sintering of Ag nanoparticles for high-power density electronic packaging. *Scr. Mater.* 69, 789 (2013).

29. H. Zhang, H. Bai, P. Peng, W. Guo, G. Zou, and L. Liu, SiC chip attachment sintered by nanosilver paste and their shear strength evaluation. *Weld. World* 63, 1055 (2019).
30. J. Dai, J. Li, P. Agyakwa, M. Corfield, and C.M. Johnson, Shear strength of die attachments prepared using dry nanosilver film by a time-reduced sintering process. *Microelectron. Reliab.* 111, 113740 (2020).
31. J. Dai, J. Li, P. Agyakwa, M. Corfield, and C.M. Johnson, Reliability and characterization of nanosilver joints prepared by a time-reduced sintering process; reliability and characterization of nanosilver joints prepared by a time-reduced sintering process. *IEEE Trans. Device Mater. Reliab.* 21(4), 536 (2021).
32. U. Scheuermann and R. Schmidt, Impact of solder fatigue on module lifetime in power cycling tests, Proceedings of the 2011 14th European Conference on Power Electronics and Applications, Birmingham, UK, pp. 1–10 (2011).
33. T. Herrmann, M. Feller, J. Lutz, R. Bayerer, and T. Licht, Power cycling induced failure mechanisms in solder layers, 2007 European Conference on Power Electronics and Applications, Aalborg, Denmark, pp. 1–7, (2007).
34. J. Li, J. Dai, and C.M. Johnson, Comparison of power cycling reliability of flexible PCB interconnect smaller/thinner and larger/thicker power devices with topside Sn-3.5Ag solder joints. *Microelectron. Reliab.* 84, 55 (2018).
35. A.A. Bajwa and J. Wilde, Reliability modeling of Sn-Ag transient liquid phase die-bonds for high-power SiC devices. *Microelectron. Reliab.* 60, 116 (2016).
36. F. Yang, W. Zhu, W. Wu, H. Ji, C. Hang, and M. Li, Microstructural evolution and degradation mechanism of SiC–Cu chip attachment using sintered nano-Ag paste during high-temperature ageing. *J. Alloys Compd.* 846, 156442 (2020).
37. Y.Z. Hu, R. Sharangpani, and S.-P. Tay, In situ rapid thermal oxidation and reduction of copper thin films and their applications in ultralarge scale integration. *J. Electrochem. Soc.* 148, G669 (2001).
38. Q. Zhang, A. Zehri, J. Liu, W. Ke, S. Huang, M.G. Latorre, N. Wang, X. Lu, C. Zhou, W. Xia, Y. Wu, L. Ye, and J. Liu, Mechanical property and reliability of bimodal nano-silver paste with Ag-coated SiC particles. *Solder. Surf. Mt. Technol.* 31(4), 193 (2019).
39. R.O. Ritchie, Mechanisms of fatigue crack propagation in metals, ceramics and composites: role of crack tip shielding*. *Mater. Sci. Eng. A* 103(1), 15 (1988).
40. C. Chen, Z. Zhang, D. Kim, B. Zhang, M. Tanioku, T. Ono, K. Matsumoto, and K. Suganuma, Interfacial oxidation protection and thermal-stable sinter Ag joining on bare Cu substrate by single-layer graphene coating. *Appl. Surf. Sci.* 497, 143797 (2019).
41. P. Peng, A. Hu, A.P. Gerlich, G. Zou, L. Liu, and Y.N. Zhou, Joining of silver nanomaterials at low temperatures: processes, properties, and applications. *ACS Appl. Mater. Interfaces* 7, 12597 (2015).
42. M. Schaal, M. Klingler, and B. Wunderle, Silver Sintering in Power Electronics: The State of the Art in Material Characterization and Reliability Testing, 2018 7th Electronic System-Integration Technology Conference (ESTC), Dresden, Germany pp. 1–18 (2018).
43. T. Herboth, M. Guenther, A. Fix, and J. Wilde, Failure mechanisms of sintered silver interconnections for power electronic applications, 2013 IEEE 63rd Electronic Components and Technology Conference, Las Vegas, NV, USA, 2013, pp. 1621–1627 (2013).
44. J.G. Bai, T.G. Lei, J.N. Calata, and G.Q. Lu, Control of nanosilver sintering attained through organic binder burnout. *J. Mater. Res.* 22, 3494 (2007).
45. H. Zhang, W. Wang, H. Bai, G. Zou, L. Liu, P. Peng, and W. Guo, Microstructural and mechanical evolution of silver sintering die attach for SiC power devices during high temperature applications. *J. Alloys Compd.* 774, 487 (2019).
46. S. Mishra and T. DebRoy, Non-isothermal grain growth in metals and alloys. *Mater. Sci. Technol.* 22(3), 253 (2006).
47. R.D. Doherty, D.A. Hughes, F.J. Humphreys, J.J. Jonas, D.J. Jensen, M.E. Kassner, W.E. King, T.R. Mcnelleny, H.J. Mcqueen, and A.D. Rollett, Current issues in recrystallization: a review. *Mater. Sci. Eng. A* 238(2), 219 (1997).
48. C. Choe, S. Noh, C. Chen, D. Kim, and K. Suganuma, Influence of thermal exposure upon mechanical/electrical properties and microstructure of sintered micro-porous silver. *Microelectron. Reliab.* 88–90, 695 (2018).
49. T. Suzuki, T. Terasaki, Y. Kawana, D. Ishikawa, M. Nishimura, H. Nakako, and K. Kurafuchi, Effect of manufacturing process on micro-deformation behavior of sintered-silver die-attach material. *IEEE Trans. Device Mater. Reliab.* 16, 588 (2016).
50. D. Kim, S. Lee, C. Chen, S.J. Lee, S. Nagao, and K. Suganuma, Fracture mechanism of microporous Ag-sintered joint in a GaN power device with Ti/Ag and Ni/Ti/Ag metallization layer at different thermo-mechanical stresses. *J. Mater. Sci.* 56, 9852 (2021).
51. H. H. Hausner, Grain growth during sintering. Vol. 154. United States Atomic Energy Commission, Technical Information Service (1954).
52. B. Günther, A. Kumpmann, and H.-D. Kunze, Secondary recrystallization effects in nanostructured elemental metals. *Scr. Metall.* 27(7), 833 (1992).
53. T.H. Chuang, C.H. Tsai, H.C. Wang, C.C. Chang, C.H. Chuang, J. der Lee, and H.H. Tsai, Effects of annealing twins on the grain growth and mechanical properties of Ag-8Au-3Pd bonding wires. *J. Electron. Mater.* 41, 3215 (2012).
54. C. Chen, C. Choe, Z. Zhang, D. Kim, and K. Suganuma, Low-stress design of bonding structure and its thermal shock performance (– 50 to 250°C) in SiC/DBC power die-attached modules. *J. Mater. Sci. Mater. Electron.* 29, 14335 (2018).
55. F. Yang, B. Hu, Y. Peng, C. Hang, H. Chen, C. Lee, J. Wei, and M. Li, Ag microflake-reinforced nano-Ag paste with high mechanical reliability for high-temperature applications. *J. Mater. Sci. Mater. Electron.* 30, 5526 (2019).
56. Z. Zhu, Y. Chan, and F. Wu, Effect of alternating current (AC) stressing on the microstructure and mechanical properties of low-silver content solder interconnect. *Microelectron. Reliab.* 92, 12 (2019).
57. H. Zhang, C. Chen, S. Nagao, and K. Suganuma, Thermal fatigue behavior of silicon-carbide-doped silver microflake sinter joints for die attachment in silicon/silicon carbide power devices. *J. Electron. Mater.* 46, 1055 (2017).
58. T. Suzuki, Y. Yasuda, T. Terasaki, T. Morita, Y. Kawana, D. Ishikawa, M. Nishimura, H. Nakako, K. Kurafuchi, and T. Matsuda, Evaluation of Microscopic Strain Distribution of Low-Temperature Sintering Die Attach in Thermal Cycling Test, 2018 20th International Conference on Electronic Materials and Packaging (EMAP), Hong Kong, China, pp. 1–4 (2018).
59. M. Wang, Y. Mei, X. Li, R. Burgos, D. Boroyevich, and G.Q. Lu, How to determine surface roughness of copper substrate for robust pressureless sintered silver in air. *Mater. Lett.* 228, 327 (2018).
60. M. Usui, M. Ishiko, K. Hotta, S. Kuwano, and M. Hashimoto, Effects of uni-axial mechanical stress on IGBT characteristics. *Microelectron. Reliab.* 45(9–11), 1682 (2005).
61. A. Turnbull, E.R. De, and L. Rios, Predicting fatigue life in commercially pure aluminium using a short crack growth model. *Fatigue Fract. Eng. Mater. Struct.* 18, 1469 (1995).

Publisher's Note Springer Nature remains neutral with regard to jurisdictional claims in published maps and institutional affiliations.

Authors and Affiliations

Pearl A. Agyakwa¹  · Stuart Robertson² · Jingru Dai¹ · Bassem Mouawad¹ · Zhaoxia Zhou² · Changqing Liu³ · C. Mark Johnson¹

✉ Pearl A. Agyakwa
pearl.agyakwa@nottingham.ac.uk

¹ The University of Nottingham, University Park,
Nottingham NG7 2RD, UK

² Loughborough Materials Characterisation Centre,
Department of Materials, Loughborough University,
Loughborough, Leicestershire LE11 3TU, UK

³ Wolfson School of Mechanical, Electrical
and Manufacturing Engineering, Loughborough University,
Loughborough, Leicestershire LE11 3TU, UK